Progress in Oceanography 123 (2014) 1–23

Contents lists available at ScienceDirect

Progress in Oceanography

journal homepage: www.elsevier.com/locate/pocean

Mineralization of biogenic materials in the water masses of the South Atlantic Ocean. I: Assessment and results of an optimum multiparameter analysis

M. Álvarez [a,*], S. Brea [b], H. Mercier [c], X.A. Álvarez-Salgado [b]

[a] Instituto Español de Oceanografía, Centro de A Coruña, Apdo. 130, 15080 A Coruña, Spain
[b] IIM (CSIC), Eduardo Cabello 6, 36208 Vigo, Spain
[c] LPO (IFREMER), B.P. 70, Plouzane, 29280 Brest, France

ARTICLE INFO

Article history:
Available online 8 January 2014

ABSTRACT

This is the first of two manuscripts dealing with the circulation, mixing, ventilation and organic matter mineralization of the South Atlantic Ocean (SAO). The present work quantifies the complex mixing of water masses in the SAO using a constrained, least-squares regression, Optimum MultiParameter (OMP) analysis. The OMP based on temperature, salinity, silicate and the conservative parameter NO, was applied on two World Ocean Circulation (WOCE) lines, A17 and A14, in the western and eastern SAO, respectively. The constrained OMP sensitivity to sources of error in the end-member characteristics, measured parameters, equation weights and oxygen to nitrogen mineralization ratio (R_N) was carefully assessed using perturbation tests. Perturbation of R_N was the only test that changed significantly the mixing proportions although by less than 5%. The constrained OMP method allowed defining the realm and identifying the core-of-flow of each water mass to study its circulation, the evolution of its chemical composition and, eventually, to separate the contribution of physical and biogeochemical processes. Relevant specific outputs of this first manuscript are: (1) north of the South Equatorial Current, the silicate maximum is primarily composed of Antarctic Intermediate Water (AAIW) rather than Circumpolar Deep Water (CDW); (2) the two degree discontinuity (TDD) experiences a dramatic meridional change of water masses composition, being dominated by North Atlantic Deep Water (NADW) north of the Vema Channel and by CDW southwards; (3) the 50% proportion horizon of Weddell Sea Deep Water (WDSW), with a θ of −0.3 °C at the entry of the SAO, defines the upper limit of the WSDW realm more properly than the classical isopycnals of 46.04 or 46.06 σ_4, where the proportion of WSDW is around 75%.

1. Introduction

This work is the first part of a study with the general aim of assessing the lability of the mineralized biogenic materials, the corresponding mineralization rates, and the close relationship between lability and mineralization for the different water masses that circulate and mix in the South Atlantic Ocean (SAO) using a geochemical approach. Two high quality and densely-sampled World Ocean Circulation Experiment (WOCE) lines, A14 and A17 (Fig. 1), will be used for attaining our objectives.

The particular aims of this manuscript are: (1) to set and carefully assess the Optimum MultiParameter (OMP) analysis (Tomczak, 1981) used to solve the complex mixing of water masses in the SAO; and (2) to provide new insight on the distribution of those water masses not yet resolved by the classical approach based on the meridional and/or zonal evolution of extremes in the thermohaline and chemical parameters.

The OMP is considered a relatively simple inverse method to reconstruct distributions of water mass mixing compared to more complex physical models (e.g., Marsh et al., 2000; Speich et al., 2002). This method has been widely used in the oceanographic literature to investigate water mass distributions in diverse regions of the oceans (www.ldeo.columbia.edu/~jkarsten/omp_std/, e.g., You, 1997; Castro et al., 1998; Pérez et al., 2001; de Brauwere et al., 2007; Johnson, 2008) and to resolve nutrient mineralization and oxygen utilization patterns (Hupe and Karstensen, 2000; Pérez et al., 2001; Thomas and Ittekkot, 2001; Brea et al., 2004), the temporal variability of water masses (Henry-Edwards and Tomczak, 2006), or the water mass ages and anthropogenic carbon storage (Karstensen and Tomczak, 1998; Thomas and Ittekkot, 2001).

The main advantage of the OMP analysis is its relative simplicity and few assumptions; additionally, the resulting water mass mixing fractions are directly visualizable and interpretable. Despite this, several shortcomings should be kept in mind when using an OMP method:

* Corresponding author. Tel.: +34 981218171.
E-mail address: marta.alvarez@co.ieo.es (M. Álvarez).

0079-6611/$ - see front matter © 2014 Elsevier Ltd. All rights reserved.
http://dx.doi.org/10.1016/j.pocean.2013.12.007

List of acronyms

AABW	Antarctic Bottom Water
AAIW	Antarctic Intermediate Water
ACC	Antarctic Circumpolar Current
BC	Brazil Current
BCF	Brazil Current Front
CARINA	CARbon IN Atlantic ocean, http://cdiac.ornl.gov/oceans/CARINA/Carina_inv.html
CCHDO	CLIVAR and Carbon Hydrographic Data Office, http://whpo.ucsd.edu/
CDW	Circumpolar Deep Water, Upper (UCDW) and Lower (LCDW)
CITHER	CIrculation THERmohaline
DWBC	Deep Western Boundary Current
ECS	Equatorial Current System
GLODAP	Global Ocean Data Analysis Project, http://cdiac.ornl.gov/oceans/glodap/Glodap_home.htm
MC	Malvinas Current
MF	Malvinas Front
NADW	North Atlantic Deep Water, Upper (UNADW), Middle (MNADW) and Lover (LNADW)
NBC	North Brazil Current
NECC	North Equatorial CounterCurrent
NEUC	North Equatorial UnderCurrent
NICC	North Intermediate CounterCurrent
NNLS	Non-Negative Least Squares
OMP	Optimum MultiParameter analysis
R/V	Research Vessel
SAC	South Atlantic Current
SACW	South Atlantic Central Water
SAF	Sub-Antarctic Front
SAMW	Sub-Antarctic Mode Water
SAO	South Atlantic Ocean
SAZ	Sub-Antarctic Zone
SEC	South Equatorial Current
SECC	South Equatorial CounterCurrent
SEG	Sub-Equatorial Gyre
SICC	South Intermediate CouterCurrent
SMW	Salinity Maximum Water
SOCS	Southern Ocean Carbon Synthesis group
STF	Sub-Tropical Front
STG	Sub-Tropical Gyre
STMW	Sub-Tropical Mode Water
SWT	Source Water Type
TDD	Two Degree Discontinuity
WOCE	World Ocean Circulation Experiment
WSDW	Weddell Sea Deep Water

(1) A sample is supposed to be the result of the linear mixing of several Source Water Types (SWT). Therefore, first we need to select which SWT define a sample and, second, which are their physical and chemical characteristics that are supposed to be constant with time in the formation area.
(2) To solve the system of linear equations, the number of unknowns (SWT fractions, n_{SWT}) may not exceed the number of variables (n_{var}) considered plus one. If $n_{SWT} > n_{var} + 1$ we have a system with infinite solutions, ill posed; if $n_{SWT} = n_{var} + 1$ just one solution correctly satisfies the system. This unique solution would be of little statistical significance because there are not residual degrees of freedom. If $n_{SWT} < n_{var} + 1$, the system is over-determined.
(3) Another issue to take into account is the differential weighting of the parameters and mass conservation equations. Some parameters are difficult to measure and have a low instrumental or analytical accuracy; others may vary more in time and space and are therefore affected by a large

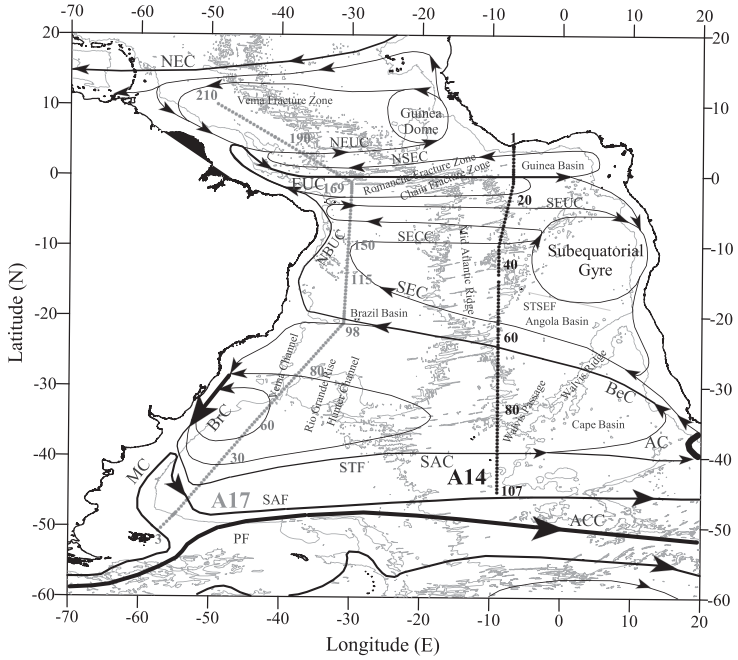

Fig. 1. Chart of the South Atlantic Ocean showing the stations occupied by WOCE line A14 and A17. Major features of the wind–driven upper ocean circulation (100–500 m depth range) are shown (adapted from Stramma and England, 1999; and Stramma and Schott, 1999). The −4000 m isobath is also included, to separate the South Atlantic deep basins. AC, Agulhas Current; ACC, Antarctic Circumpolar Current; BrC, Brazil Current; BeC, Benguela Current; EUC, Equatorial Under Current; MC, Malvinas (Falkland) Current; NBUC, North Brazil Under Current; NEC, North Equatorial Current; NEUC, North Equatorial Under Current; NSEC, North South Equatorial Current; SAC, South Atlantic Current, SECC, South Equatorial Counter Current; SEUC, South Equatorial Under Current; SEC, South Equatorial Current and; STSEF, SubTropical–SubEquatorial Front.

environmental variability. To account for these differences, all parameters have to be weighted. The weighting procedure suggested in the OMP user group web page is that from Tomczak and Large (1989): for each parameter, the weight is calculated as its variance in the SWT matrix divided by the largest variance of the parameter in the source region. Further choices can be made to account for the relative influence of each SWT parameter in the solution (e.g., de Brauwere et al., 2007; Johnson, 2008). The highest weight is generally assigned to the mass conservation equation, as it represents a physical constraint instead of a linear mixing equation (de Brauwere et al., 2007).

This work is primarily a methodological study to assess the reliability of a classical OMP analysis performed in the SAO to resolve its complex water mass mixing patterns. Several sensitivity analyses will be performed to check the stability of the resulting water mass distributions, which will be finally discussed. In addition, the meridional evolution of the thermohaline and chemical properties along the core-of-flow, i.e. the lines of maximum proportions, of the different SWT, will be examined.

2. Data set

WOCE line A17 (Fig. 1) was occupied during the cruise CITHER (Circulation THERmohaline)-2, aboard R/V *Maurice Ewing*, from 4 January to 21 March 1994. WOCE line A14 (Fig. 1) was sampled during the first leg of cruise CITHER-3, aboard R/V *l'Atalante*, from 11 January to 16 February 1995. The WOCE A17 hydrographic and biogeochemical parameters of the WOCE Hydrographic Programme were measured at 235 full-depth stations from 10°N to 52°S, at a nominal distance of 600 km from the continental slope. A general presentation of the A17 cruise and the complete database can be found in volumes 1–3 of the CITHER-2 data report (Groupe CITHER-2, 1995, 1996a,b). In the case of WOCE A14, hydrographic and biogeochemical parameters were measured at 107 full-depth stations from 4°N to 45°S, along ~9°W. A general presentation of the cruise and the complete database can be found in volumes 2 and 3 of the CITHER-3 data report (Groupe CITHER-3, 1996, 1998).

The parameters used in the present work (salinity, temperature, dissolved oxygen, nitrate, phosphate, silicate and chlorofluorocarbon 11) were measured on both cruises at a maximum of 32 levels using standard methods, which are explained in detail in the data reports. The original data can be found in the CCHDO (CLIVAR and Carbon Hydrographic Data Office) web site (http://whpo.ucsd.edu/). Both cruises were incorporated to GLODAP (Global Ocean Data Analysis Project, http://cdiac.ornl.gov/oceans/glodap/Glodap_home.htm) (Key et al., 2004) and subject to a careful quality control analysis (Gouretski and Jancke, 2001).

The CARINA (CARbon IN Atlantic ocean) data synthesis is a recent effort compiling old and recent CO_2 and CO_2-relevant data from the Arctic, Atlantic and Southern Oceans (Key et al., 2010). Apart from retrieving and collecting previously unavailable data, the main aim is to obtain a consistent and high-quality data base. In order to do this, a careful crossover analysis was performed on the new and reference (some original WOCE lines) data and final adjustments were suggested for particular cruises and variables (Tanhua et al., 2010).

The original WOCE A14 and A17 data were analyzed by the Southern Ocean Carbon Synthesis (SOCS) group for the Atlantic sector (Hoppema et al., 2009). Silicate for the WOCE A17 line should be multiplied by 0.98 and phosphate for the WOCE A14 by 1.02. These factors are incorporated in the original data sets used in the series of works proposed here.

3. OMP analysis

Briefly, the OMP method consists in quantifying the mixture of a set of SWT that contribute to a given water parcel/sample. The mixing is solved by minimizing the residuals of a set of linear mixing equations for conservative (classical OMP) and non-conservative (extended OMP) variables in a Non-Negative Least Squares (NNLS) sense, where mass is stringently conserved and the contributions of the different SWT must be positive.

Applying an OMP analysis to the SAO is particularly challenging. This ocean is unique in its collection of diverse water masses (Fig. 2, Table 1). A water mass is a body of water with a common formation history, having its origin in a particular region of the ocean and with physical and chemical properties distinct from the surrounding (Tomczak, 1999). A SWT is a mathematical definition, a point in a n-dimensional parameter space, a combination of temperature, salinity, nutrients, oxygen and other tracer values in the water mass formation region. According to Tomczak (1999), a water mass can be either defined by only a SWT with several parameters and the corresponding standard deviations, or in the case of Central Waters, with tight relationships between temperature and salinity, by two or more SWT.

3.1. OMP general description

The parameters that we have used to define the SWT space are four: potential temperature (θ), salinity (S), silicate (SiO_4) and the tracer NO ($NO = O_2 + R_N \cdot NO_3$, Broecker, 1974). SiO_4 is included to solve the water masses mixing below the thermocline, assuming that it behaves conservatively (Anderson and Sarmiento, 1994; Holfort and Siedler, 2001). The stoichiometric ratio R_N has been set to a constant value of 9.3 mol O_2 mol N^{-1} (Laws, 1991; Anderson, 1995; Fraga et al., 1998). Therefore, the set of mixing equations to solve is:

$$\begin{aligned}
&\sum_i x_{ij} \cdot \theta_i = \theta_j \\
&\sum_i x_{ij} \cdot S_i = S_j \\
&\sum_i x_{ij} \cdot (NO)_i = (NO)_j \\
&\sum_i x_{ij} \cdot (SiO_4)_i = (SiO_4)_j \\
&\sum_i x_{ij} = 1
\end{aligned} \tag{1}$$

where the subscript i corresponds to each SWT and j to every sample and x_{ij} are the SWT fractions. The last row stands for the mass conservation condition. In matrix notation the formulation will be:

$$A \cdot X = N \tag{2}$$

where A is the (5×13) matrix with the physical and chemical SWT characteristics (Table 2), X is the $(13 \times n)$ matrix with the SWT fractions, N is the $(5 \times n)$ matrix with the measured variables, n being the number of samples.

The linear mixing equations are normalized and weighted. The normalization is done using the mean and standard deviation values for the four parameters in the SWT matrix (Table 2). In addition, equations are weighted taking into account the ratio between the standard deviation of each parameter in the SWT matrix and the uncertainty of the estimation of that water type parameter. Weights of 8, 4, 2 and 1 were assigned to θ, S, NO and SiO_4, respectively. A weight of 100 was assigned to the mass conservation equation, i.e., we have assumed that the mass is accurately conserved.

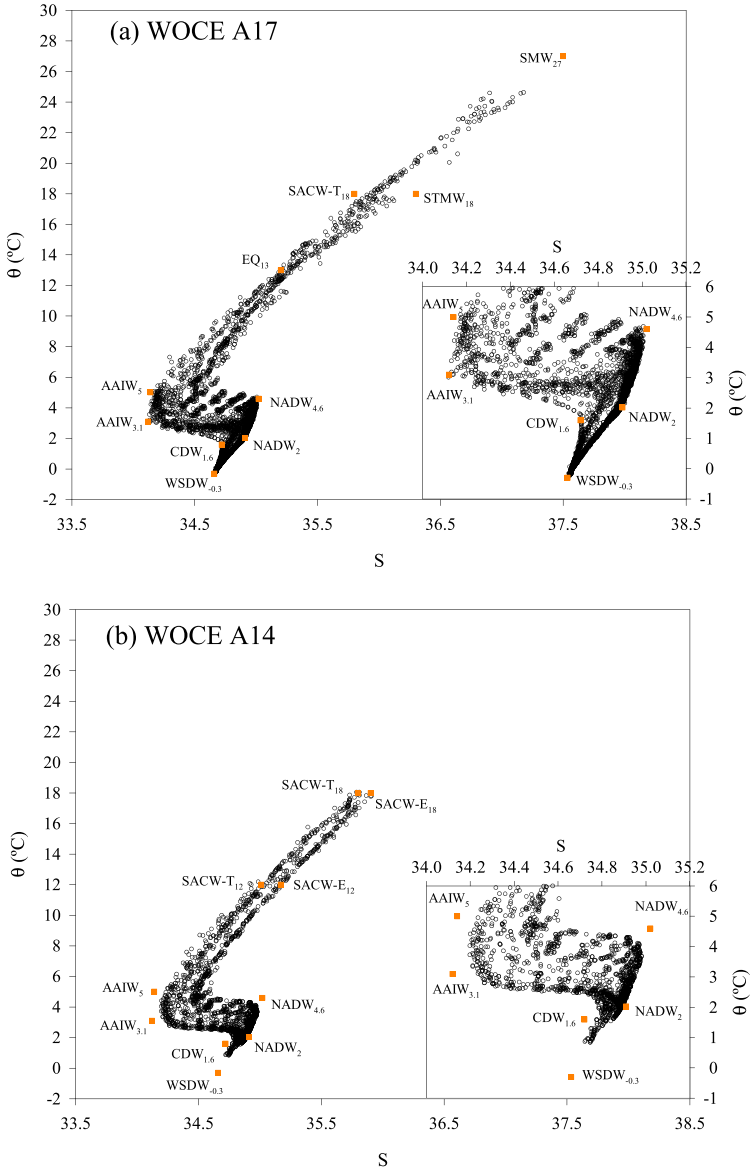

Fig. 2. Potential temperature (θ, °C)–salinity (S, psu) diagram for (a) the WOCE A17 and (b) WOCE A14 lines. The orange symbols stand for the thermohaline properties of the SWT considered. (For interpretation of the references to colour in this figure legend, the reader is referred to the web version of this article.)

3.2. Water masses and their properties

In this section we will describe the water masses present in the SAO and the physical and chemical characteristics of the SWT selected to solve the mixing analysis. The water masses in the SAO were separated into Central, Intermediate, Deep and Bottom (Table 1). The physical properties, temperature and salinity, were taken from the literature and the chemical properties, NO and SiO_4, were estimated from a linear regression analysis of the property versus salinity or temperature within the realm of the corresponding water mass. Following Poole and Tomczak (1999), the standard error of these regression equations have been used to compute the uncertainty in the estimation of the water type characteristics (Table 2).

3.2.1. Central Water masses

The term Central Water is used to define the water masses subducted into the thermocline (Tomczak and Godfrey, 2003). In the case of the SAO, South Atlantic Central Water (SACW) comprises three mode waters: Salinity Maximum Water (SMW), Sub-Tropical Mode Water (STMW) and Sub-Antarctic Mode Water (SAMW).

The SMW is the warmest modal water mass of the SAO (~27 °C), formed by evaporation between 12°S and 22°S (Worthington, 1976). The SMW is transported by the South-Equatorial Current (SEC) towards the American coast, where it is transported north and southwards within the boundary currents.

The STMW forms in the subtropical gyre (Gordon, 1981). Provost et al. (1999) defined three types of STMW covering a range of temperatures between 12 °C and 18 °C. The dominant mode of 14–16 °C forms in the southern part of the Brazil current recirculation region. It extends eastwards beyond 25°W (Tsuchiya et al., 1994), mainly within its outcropping region between 42°S and 34°S (Mémery et al., 2000), and subducts towards the Equator north and south of the line of vanishing heat flux into the ocean (Mémery et al., 2000). Within this region, inshore of line A17, a warm type of STMW of ~18 °C, forms around 35°S in the inner recirculation of the Brazil current.

The SAMW forms north of the SubAntarctic Front (SAF) by winter convection (McCartney, 1977, 1982). The areas with the deepest winter mixed layers in the SAF are the South-East Indian and South-East Pacific oceans, just west of the Drake Passage (Hanawa and Talley, 2001; Aoki et al., 2007).

Table 1
Main water masses of the SAO with a brief description of their characteristics and some references where more information about their origin and circulation can be found. The Source Water Types used to model them are shown.

	Name and acronym	Source	Characteristics	SWT	References
Central	Salinity Maximum Water (SMW)	Tropical area (12–22°S)	Warmest (~27 °C) mode water in the SAO, formed by evaporation, transported westward to America with SEC	SMW_{27}	Worthington (1976), Stramma and England (1999) and Mémery et al. (2000)
	Sub-Tropical Mode Water (STMW)	Subtropical gyre (42–34°S)	Mode water with a range of temperatures from 12 to 18 °C, thickest and warmest mode formed in the southern area of Brazil current	$STMW_{18}$	Gordon (1981), Provost et al. (1999) and Mémery et al. (2000) and Mémery et al. (2000)
	Equatorial 13 °C water (EQ)	Eastern SAO, near Namibia	Formed by vertical mixing of low salinity water outcropped further south with the overlying high-salinity water. Transported NW with SEC, flows to the Equator along the Brazilian coast with NBC	EQ_{13}	Tsuchiya (1986)
	Equatorial South Atlantic Central Water (SACW-E)	Western Tropical area	Series of mode waters formed north of the Angola-Benguela front (~18°S) within the Angola Dome. Higher salinity, lower oxygen than SACW-T	$SACW\text{-}E_{18}$ $SACW\text{-}E_{12}$	Gordon and Bosley (1991)
	Subtropical South Atlantic Central Water (SACW-T)	Western Subtropical gyre	Series of mode waters formed south of the Angola-Benguela front (~18°S)	$SACW\text{-}T_{18}$ $SACW\text{-}T_{12}$	Gordon and Bosley (1991)
Intermediate	Antarctic Intermediate Water (AAIW)	Pacific Oc. north SAF & Malvinas - Brazil current	Formed by ventilation of SAMW in both areas, characterized by a salinity minimum and oxygen maximum north of the SAF	$AAIW_5$ $AAIW_3$	McCartney (1982), Piola and Gordon (1989) and Talley (1996)
Deep	Circumpolar Deep Water (CDW)	Antarctic Circumpolar Current	Also named Common Water, formed by mixing in ACC of mid-depth Indian, Pacific and Atlantic deep water with WSBW and NADW	$CDW_{1.6}$	Montgomery (1958), Georgi (1981) and Broecker et al. (1985)
	North Atlantic Deep Water (NADW)	North Atlantic Ocean	Carried into SAO with DWBC. Characterized by salinity maximum; upper by a silicate minimum; middle and lower by oxygen maxima	$NADW_{4.6}$ $NADW_2$	Wüst (1935), Speer and McCartney (1992) and Friedrichs et al. (1994)
Bottom	Weddell Sea Deep Water (WSDW)	Weddell Sea	Formed by mixing of WSBW and WDW (1:1), coldest water in SAO, nutrient rich and oxygen poor	$WSDW_{-0.3}$	Reid (1989), Onken (1995) and Arhan et al. (1999)

Table 2
Matrix with the physical and chemical characteristics (value ± uncertainty) of the 13 Source Water Types used to model the water mixing in the SAO. The correlation coefficient (r^2), the standard deviation of the residuals (std.res.) and the number of data (n) of the back-calculated versus measured variables are also shown.

SWT	θ (°C)	S	NO (μmol kg^{-1})	SiO_4 (μmol kg^{-1})
SMW_{27}	27.0 ± 0.1	37.50 ± 0.01	206 ± 3	1.1 ± 0.5
$STMW_{18}$	18.0 ± 0.1	36.30 ± 0.01	235 ± 3	1.3 ± 0.5
EQ_{13}	13.0 ± 0.1	35.20 ± 0.01	315 ± 3	5.3 ± 0.7
$SACW\text{-}E_{18}$	18.0 ± 0.1	35.90 ± 0.01	261 ± 3	3.4 ± 0.7
$SACW\text{-}E_{12}$	12.0 ± 0.1	35.17 ± 0.01	331 ± 3	10.1 ± 0.7
$SACW\text{-}T_{18}$	18.0 ± 0.2	35.80 ± 0.02	221 ± 4	1.5 ± 0.5
$SACW\text{-}T_{12}$	12.0 ± 0.2	35.01 ± 0.02	327 ± 4	3.6 ± 0.5
$AAIW_5$	5.00 ± 0.08	34.14 ± 0.01	482 ± 3	7.0 ± 0.7
$AAIW_3$	3.10 ± 0.08	34.12 ± 0.01	558 ± 3	16.4 ± 0.7
$CDW_{1.6}$	1.60 ± 0.03	34.720 ± 0.003	497 ± 1	110.6 ± 0.9
$NADW_{4.6}$	4.6 ± 0.1	35.020 ± 0.005	426 ± 2	7.3 ± 0.5
$NADW_2$	2.02 ± 0.03	34.910 ± 0.003	446 ± 1	28.2 ± 0.9
$WSDW_{-0.3}$	−0.30 ± 0.03	34.660 ± 0.001	543 ± 2	135.5 ± 2
r^2	0.99997	0.9994	0.998	0.9995
Std.res.	±0.02	±0.008	±3	±0.7
n	7211	7211	7211	7211

According to Tsuchiya (1986), the original type of Equatorial water of 13 °C is formed in the thermocline of the eastern SAO near Namibia by vertical mixing of dense, low-salinity water from the winter outcrop further south and overlying less dense, high-salinity water. The original 13 °C water is transported northwestward along the northern edge of the subtropical gyre and fed into the North Brazilian current, flowing equatorwards along the coast of Brazil. In the Equator, the Equatorial Undercurrent and the subsurface North and South Equatorial countercurrents branch off the North Brazilian Current and transport the 13 °C water eastwards. There is also a westward return flow on both sides of the undercurrent, spreading the 13 °C water over the thermostad region.

In the eastern SAO, the Angola-Benguela front, located around 18°S, separates two thermocline regimes: higher salinities, about 0.1, and lower oxygen values are found north of the front within the cyclonic gyre of the Angola Dome (Gordon and Bosley, 1991). This front separates subequatorial from subtropical SACW.

In this work, Central Waters in the western SAO have been modelled by three SWT: SMW_{27}, $STMW_{18}$ and EQ_{13} (Tables 1 and 3). Additionally, the warmest subtropical type, $SACW\text{-}T_{18}$, is shared with the eastern SAO. In the case of the eastern SAO, Central Waters have been separated into subequatorial and subtropical and four SWT have been used to model them: $SACW\text{-}T_{18}$, $SACW\text{-}T_{12}$, $SACW\text{-}E_{18}$ and $SACW\text{-}E_{12}$ (Tables 1 and 3).

3.2.2. Intermediate Water masses

The main Intermediate Water in the SAO is Antarctic Intermediate Water (AAIW), formed north of the SAF and east of the Drake Passage by ventilation of SAMW (McCartney, 1977, 1982). AAIW is characterized by a salinity minimum and oxygen maximum. There are two distinct types of AAIW: the one produced west of Drake Passage and entering the South Pacific subtropical gyre by subduction, and the one produced east of Drake Passage in the confluence of the Malvinas and Brazil currents (Talley, 1996). The first

type corresponds to the coldest SAMW variety of the South Pacific colder than 4.5 °C. SAMW formed in the southeast Pacific and Scotia Sea appears to cross the Drake Passage and turn north past the Malvinas Islands into the SAO, where it contributes to AAIW in this ocean (McCartney, 1977). Accordingly, Piola and Gordon (1989) have identified two AAIW end members north of Drake Passage that we have used here to model the AAIW. The lightest type ($AAIW_5$) coincides with the coldest type of SAMW identified by Piola and Gordon (1989) in the Subantarctic zone and northern Drake Passage, and constitutes the primary type of AAIW in the SAO. The thermohaline and chemical characteristics of the second type ($AAIW_3$) have been taken from the southernmost stations of WOCE line A17 in the western SAO (Mémery et al., 2000).

3.2.3. Deep Water masses

The two main Deep Water masses in the SAO are the northward flowing Circumpolar Deep Water (CDW) and the southward flowing North Atlantic Deep Water (NADW). CDW is the most extensive water mass found in the Antarctic Circumpolar Current (ACC), also known as Common Water (Montgomery, 1958). CDW is not formed in contact with the atmosphere by ventilation, but by mixing of waters entering the Antarctic from mid-depths in the Indian, Pacific and Atlantic (30%) with Weddell Sea Bottom Water (45%) and deep water from the North Atlantic (25%) (Broecker et al., 1985). This explains the high nutrient and low oxygen levels of this water mass. In the southwest Atlantic, CDW splits into Upper and Lower CDW. Here, the relatively warm, salty, oxygen rich and nutrient poor NADW meets the ACC just below the oxygen minimum therein, thus splitting CDW into two parts. The upper part retains the oxygen minimum; the lower branch also shows an oxygen minimum induced by the high oxygen concentrations of the overlying NADW and the underlying bottom water. In this work we have considered the thermohaline characteristics of the CDW type in Drake Passage (Georgi, 1981; Broecker et al., 1985). As in Brea et al. (2004), we have considered a unique CDW type, allowing the OMP analysis to freely model the Upper and Lower CDW.

North Atlantic Deep Water (NADW) is carried into the SAO by the Deep Western Boundary Current (DWBC) (Speer and McCartney, 1992). Three layers of NADW can be distinguished, upper, middle and lower (e.g., Friedrichs et al., 1994). Following the classical Wüst (1935) circulation scheme, the upper NADW (UNADW) is characterized by a salinity maximum related with the contribution from Mediterranean Water, and also by a silicate minimum. Middle NADW, delivered from the central Labrador Sea, is characterized by a brief oxygen maximum. Finally, lower NADW (LNADW) originates from the overflow spill in the Denmark Strait and Iceland–Scotland sills and it is identified by another oxygen maximum. In this work, we have modelled the NADW with two SWT: $NADW_{4.6}$ and $NADW_2$. $NADW_{4.6}$ models both the upper and middle NADW, and $NADW_2$ defines the LNADW. The thermohaline and chemical characteristics (Table 2) of both types were taken from the northern end of WOCE line A17 (Mémery et al., 2000).

The $NADW_2$ characteristics coincide with the '2 °C discontinuity', a sharp change in the θ–S diagram around 2 °C and salinity 34.90 (Broecker et al., 1976), being the limit between the northward flowing Antarctic water and the southward flowing NADW, already identified by Worthington and Metcalf (1961).

3.2.4. Bottom Water masses

The main Bottom Water in the SAO is the Weddell Sea Deep Water (WSDW), formed from poorly-ventilated Weddell Sea Bottom Water and the overlying Warm Deep Water in a 1:1 ratio (Onken, 1995). WSDW occupies the abyssal depth of the SAO, being cold, oxygen-poor, and nutrient-rich (Reid, 1989). The thermohaline and chemical characteristics of the WSDW type were taken from the southwestern SAO (Arhan et al., 1999; Mémery et al., 2000).

The term Antarctic Bottom Water (AABW) usually refers to a blend of water types that originate at high latitudes by convective overturning and are substantially modified during their spreading history (Orsi et al., 1999). The two main water types forming AABW are WSDW and LCDW. AABW is detected as a sharp change in the θ–S diagram around 2 °C and a trend towards high silicate values. In fact, silicate is the best variable to detect waters of Antarctic origin in general and AABW in particular.

3.3. Mixing constraints

To resolve the mixing of n_{SWT} SWT, at least $n_{SWT} - 1$ tracers are needed. In this work, the total number of SWT is 13 (Table 2) and we use a maximum of 4 tracers plus the mass conservation equation. Therefore, a maximum of 5 SWT can be resolved simultaneously. Furthermore, SiO_4 is considered conservative only for waters below the thermocline, so a maximum of 4 SWT can be analyzed in the thermocline (see below and Table 3).

To overcome this difficulty we have used oceanographic criteria derived from the existing knowledge about water masses (see Section 3.2), their circulation (e.g., Reid, 1989, 1996; Stramma and England, 1999) and vertical distribution (e.g., Vanicek and Siedler, 2002) in the SAO. With all this information in mind, we defined mixing figures, where the OMP analysis of the samples comprised there is solved using a maximum of 5 or 4 SWT. Table 3 shows the mixing figures and the number of samples within each one. Since some of the mixing figures are overlapping, a sample that is present in more than one figure will be assigned to the figure yielding the lowest *Total Residual* from the OMP analysis (see Section 3.4).

3.4. Reliability and robustness

The reliability and robustness of the OMP analysis rely on the values of the SWT matrix (Table 2) and the mixing constraints imposed in Section 3.3 (Table 3). To check them, we have proceeded as follows: once the matrix of proportions (X) is obtained, the sample characteristics (θ, S, NO, SiO_4) can be back-calculated using A, the SWT matrix (Table 2):

$$N_{BC} = X \cdot A \tag{3}$$

where N_{BC} is the sample matrix with the back-calculated characteristics. The correlation coefficient (r^2) and the standard deviation of the residuals of the back-calculated parameters give indications of the goodness of fit or the reliability of the proposed OMP. In our case, the r^2 for all the input variables was higher than 0.996 and the standard deviation of the residuals was low (Table 2), slightly above the measurement error.

The NNLS method used to resolve the set of mixing equations (*lsqnonneg* function in Matlab®) provides the contribution of the SWT introduced, the *Total Residual* from the system of equations, and the *Individual Residual* for θ, S, NO, SiO_4, and mass conservation for each sample. The *Individual Residuals* are weighted and normalized as the equations, so they give a hint on the relative contribution of each equation to the *Total Residual*. The *Total Residual* provides an idea of how well the OMP resolves the mixing of water masses for each sample, being mathematically the squared sum of the absolute *Individual Residuals*:

$$\text{Total Residual}_j = \sum_{1}^{p} (\text{abs}(A_i \cdot x_{ij} - N_j))_p^2 \tag{4}$$

where p stands for each mixing equation or variable, i for each SWT and j for each sample, A is the SWT matrix (Table 2), x the SWT frac-

Table 3
Mixing figures used to solve the OMP analysis in the SAO. The number of samples comprised within the figure (n) is shown.

Section	Figure	SWT comprised	Variables	n
A14	1	SACW-E_{18}, SACW-E_{12}	θ, S, NO	117
	2	SACW-T_{18}, SACW-T_{12}	θ, S, NO	106
	3	SACW-E_{18}, SACW-E_{12}, SACW-T_{18}, SACW-T_{12}	θ, S, NO	20
	4	SACW-E_{12}, $AAIW_5$, $AAIW_3$, $CDW_{1.6}$, $NADW_{4.6}$	θ, S, NO, SiO_4	328
	5	SACW-T_{12}, $AAIW_5$, $AAIW_3$, $CDW_{1.6}$, $NADW_{4.6}$	θ, S, NO, SiO_4	389
A17	6	SMW_{27}, $STMW_{18}$, SACW-T_{18}	θ, S, NO	101
	7	$STMW_{18}$, EQ_{13}, SACW-T_{18}	θ, S, NO	203
	8	EQ_{13}, $AAIW_5$, $AAIW_3$, $CDW_{1.6}$, $NADW_{4.6}$	θ, S, NO, SiO_4	989
A14 + A17	9	$AAIW_5$, $AAIW_3$, $CDW_{1.6}$, $NADW_{4.6}$, $NADW_2$	θ, S, NO, SiO_4	3648
	10	$CDW_{1.6}$, $NADW_2$, $WSDW_{-0.3}$	θ, S, NO, SiO_4	1310
Total	10	13		7211

tions and N the measured variables. Remember that A and N are normalized and weighted.

The weighted and dimensionless *Individual Residuals* are converted into real residuals as follows:

$$\text{Real Residual}_j = (\text{Individual Residual}_j/W_p)\cdot(\text{STD}_p) \quad (5)$$

where the *Individual Residual* comes from the NNLS method for every sample j, and W_p is the weight applied to the corresponding equation p and STD is the standard deviation of the variable p in the SWT matrix (Table 2).

Fig. 3a shows the *Total Residual* of the OMP analysis for WOCE lines A14 and A17. The raw number has no meaning, but the vertical distribution shows the relative goodness of the OMP fitting to the data. In both cruises, the upper 500 dbar were less well modelled than the deeper water column. The layer between 2000 and 4000 dbar also presented a relative maximum in the residuals, showing an area of lower adjustment of the mixing analysis. A closer look at the *Individual Residuals* (Fig. 3b) shows that in the upper 500 dbar, all the variables contributed to the uncertainty of the mixing model, but in the layer between 2000 and 4000 dbar, the main contributors were NO and salinity.

The stability or robustness of the proposed OMP analysis was checked by means of perturbation tests (Lawson and Hanson, 1974). The physical and chemical characteristics in the SWT matrix (Table 2) were modified introducing normally distributed random numbers within the uncertainty assigned to each variable and SWT. The errors of salinity and potential temperature were estimated from the literature on basis of the current knowledge on the variability of each SWT in the source region, and the chemical errors as explained in Poole and Tomczak (1999) (Section 3.2).

A total of 100 perturbations were performed and the OMP analysis was solved for each perturbed system. Then, we calculated the mean and standard deviation (STD) of the 100 SWT distributions obtained by the perturbation analysis. The mean value has been considered the best solution retained by the OMP analysis. From the STD matrix we calculated the mean and standard deviation (Table 4) obtained which give an estimation of the stability of the system. Table 4 shows the results from the perturbation analysis, revealing that the OMP is stable, as all the mean STD were less than 1%.

3.5. Sensitivity

The sensitivity of our best OMP solution to several sources of error has been addressed by means of perturbation tests on four key components of the OMP analysis:

- The physical and chemical characteristics of the SWT introduced in the model.
- The measurement error of θ, S, NO and SiO_4.
- The weight assigned to each equation within the mixing model.
- The Redfield ratio, R_N, used to calculate the parameter NO.

On each of these tests, 100 perturbations were performed, except for the R_N variability where 31 perturbations were performed. The mean and STD of the SWT distributions and the mean *Total Residual* were calculated.

The robustness and reliability of each test was assessed in four ways: (i) the vertical variability of the mean *Total Residual*; (ii) the magnitude of the r^2 and standard deviation of the residuals of the regression between the measured and back-calculated parameters; (iii) the mean and standard deviation of the STD matrix obtained after the perturbations (the three former points were described in Section 3.4); and (iv) the percentage of samples for each SWT not significantly different from the best solution (t-student test performed at a significance level of 0.01). For any of these perturbation tests each sample was classified in the mixing figure where its *Total Residual* was minimal.

3.5.1. Test 1: variability in the SWT properties

If the SWT errors reported in Table 2 are increased 4-fold, the OMP solution still reproduced fairly well the measured variables (Table 5) but the stability of the solution decreased, especially in the Intermediate and Deep Waters (Table 4). The *Total Residual* compared to the best solution slightly increased between 4000–5000 dbars (Fig. 4). Table 6 shows the percentage of samples equal (at a significance level of 0.01) to the best solution. In this case, only the two AAIW end-members had percentages lower than 80% for both WOCE lines. In line A17, SACW-T_{18} and $WSDW_{-0.3}$ had percentages lower than 80% as well.

3.5.2. Test 2: variability in the measured variables

If the measured variables are modified with random numbers around maximum errors of 0.04 °C for θ, 0.008 for S, 2 μmol kg^{-1} for NO and 0.4 μmol kg^{-1} for SiO_4, the mean solution is nearly equal to our best solution. Here we present the results when 4-fold measurement errors are introduced.

The mean solution after these perturbations still reproduced fairly well the measured variables (Table 5), although the *Total Residual* difference showed the largest values for any of the tests (Fig. 4). The stability of this solution decreased for Intermediate and Deep Waters with maximum values in the mean STD after the perturbation tests (Table 4). The distribution of the SWT changed for intermediate (AAIW) and deep (CDW) waters on both lines (Table 6).

3.5.3. Test 3: variability in the weights

The initial weights were 8, 4, 2, and 1, for the equations of θ, S, NO and SiO_4, respectively. A weight of 100 was set to the mass conservation equation and kept constant. The other weights were

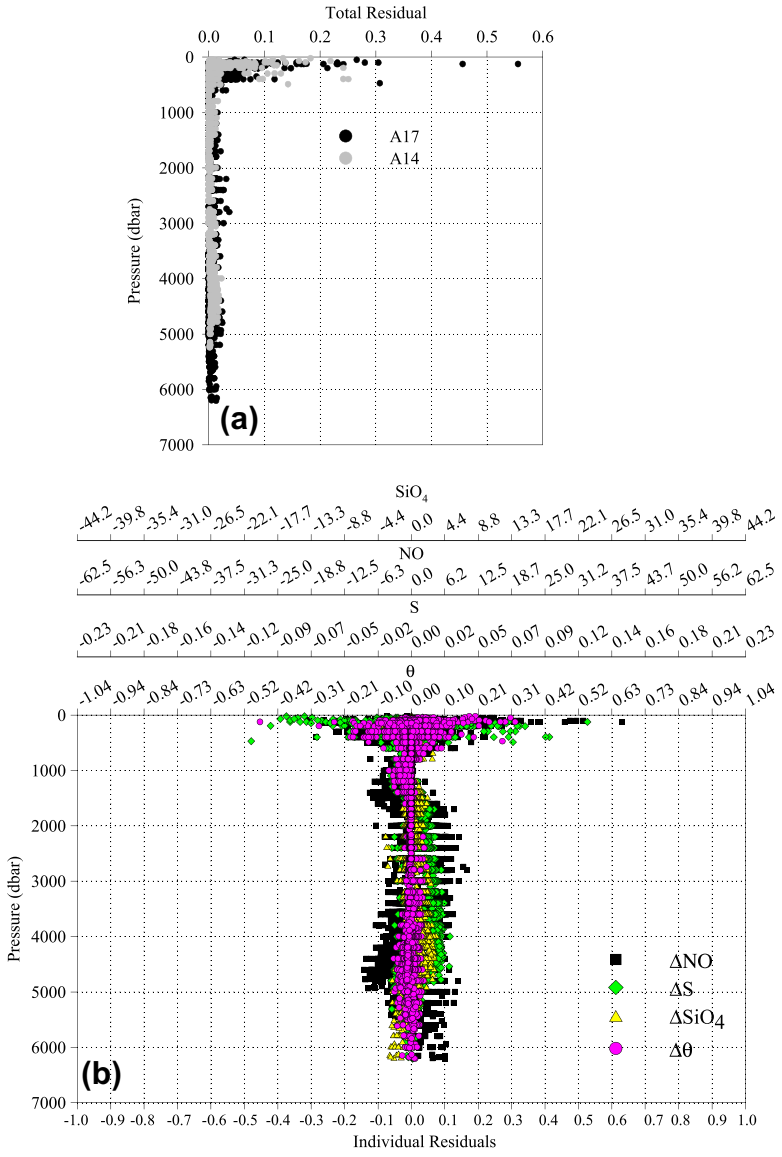

Fig. 3. (a) *Total Residual* from the mixing model and (b) *Individual Residuals* (dimensionless and weighted) from each equation introduced in the mixing analysis. The upper axes in (b) show the residuals with real units: potential temperature (θ, °C), salinity (S, psu), silicate (SiO_4, μmol kg^{-1}) and NO (μmol kg^{-1}).

modified as follows: between 11 and 6 for temperature, 7 to 2 for salinity, 5 to 1 for NO and 4 to 1 for SiO_4.

Table 4
Mean and standard deviation of the STD matrix. This matrix is obtained for each SWT contribution from the 100 or 31 perturbation tests as described in Section 3.5. Values expressed as percentages.

	Best option	SWT	Data	Weights	R_N
SMW_{27}	0.00 ± 0.04	0.02 ± 0.15	0.01 ± 0.11	0.01 ± 0.05	0.01 ± 0.05
$STMW_{18}$	0.04 ± 0.20	0.14 ± 0.73	0.13 ± 0.68	0.06 ± 0.35	0.04 ± 0.23
EQ_{13}	0.06 ± 0.13	0.23 ± 0.50	0.28 ± 0.61	0.09 ± 0.24	0.14 ± 0.39
SACW-E_{18}	0.01 ± 0.13	0.04 ± 0.39	0.04 ± 0.39	0.02 ± 0.31	0.02 ± 0.19
SACW-E_{12}	0.03 ± 0.21	0.12 ± 0.66	0.13 ± 0.63	0.04 ± 0.23	0.07 ± 0.35
SACW-T_{18}	0.05 ± 0.25	0.20 ± 0.90	0.17 ± 0.82	0.09 ± 0.55	0.06 ± 0.33
SACW-T_{12}	0.04 ± 0.22	0.17 ± 0.71	0.17 ± 0.67	0.05 ± 0.24	0.07 ± 0.31
$AAIW_5$	0.30 ± 0.48	1.17 ± 1.78	2.39 ± 3.02	0.40 ± 0.80	1.27 ± 2.44
$AAIW_3$	0.30 ± 0.47	1.15 ± 1.69	2.29 ± 2.85	0.44 ± 0.74	1.32 ± 2.52
$CDW_{1.6}$	0.30 ± 0.23	1.17 ± 0.87	2.03 ± 1.75	1.16 ± 1.10	0.41 ± 0.27
$NADW_{4.6}$	0.35 ± 0.29	1.28 ± 1.00	2.20 ± 1.53	0.47 ± 0.50	0.49 ± 0.47
$NADW_2$	0.45 ± 0.39	1.64 ± 1.35	2.73 ± 2.03	1.19 ± 1.16	0.50 ± 0.49
$WSDW_{-0.3}$	0.08 ± 0.17	0.29 ± 0.60	0.77 ± 1.52	0.14 ± 0.31	0.08 ± 0.18

The mean best solution reproduced very well the measured variables; more noise was detected reproducing SiO_4, but the NO prediction improved (Table 5). The mean *Total Residual* practically stood the same (Fig. 4). The stability was comparable to our best choice solution except for $CDW_{1.6}$ and $NADW_2$ with high STD values comparable to the SWT perturbation test (Table 4). Less than 80% of the samples were comparable to the best option for

Table 5
Correlation coefficient and standard deviation of the residuals of the back-calculated versus measured variables introduced in the OMP for the different perturbation tests.

Variable	Best option	SWT	Data	Weights	R_N
θ	0.99997 (±0.02)	0.99997 (±0.02)	0.99996 (±0.03)	0.99997 (±0.02)	0.99997 (±0.02)
S	0.9994 (±0.008)	0.9994 (±0.009)	0.9993 (±0.009)	0.9994 (±0.009)	0.9994 (±0.009)
NO	0.9976 (±3.2)	0.9976 (±3.2)	0.9975 (±3.3)	0.9979 (±3.0)	0.9938 (±3.8)
SiO_4	0.9995 (±0.7)	0.9995 (±0.7)	0.9995 (±0.7)	0.9990 (±1.0)	0.9994 (±0.8)

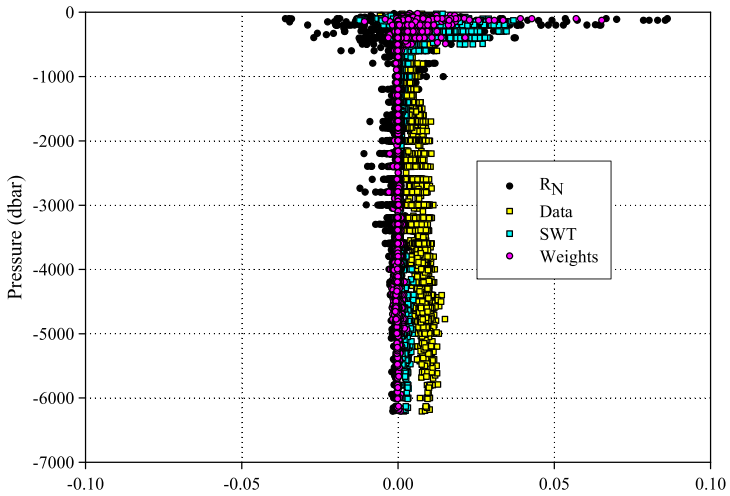

Fig. 4. Deviation of the mean *Total Residual* from each perturbation test (SWT, Data, weights and R_N) from the Best solution mean *Total Residual*, with pressure (dbar).

Table 6
Percentage and number of samples (between brackets) not significantly different from the best solution (*T*-test with $p = 0.01$) for the WOCE A14 and A17 lines. The second line shows the mean and standard deviation (in percentages) of the absolute differences between each perturbation test and the best solution, considering all the samples.

	SWT	Data	Weights	R_N
A14				
SACW-E_{18}	91 (127)	92 (129)	100 (140)	86 (121)
	0.30 ± 0.74	0.27 ± 0.58	0.10 ± 0.38	0.66 ± 1.68
SACW-E_{12}	86 (418)	80 (391)	90 (438)	38 (185)
	0.36 ± 0.89	0.31 ± 0.57	0.08 ± 0.13	0.97 ± 0.89
SACW-T_{18}	89 (113)	94 (119)	100 (127)	87 (111)
	0.38 ± 0.71	0.29 ± 0.60	0.13 ± 0.42	0.73 ± 1.79
SACW-T_{12}	81 (438)	82 (446)	99 (533)	52 (284)
	0.42 ± 0.80	0.36 ± 0.53	0.05 ± 0.09	0.77 ± 0.85
$AAIW_5$	76 (1058)	67 (942)	88 (1234)	38 (533)
	0.40 ± 0.51	0.91 ± 0.70	0.10 ± 0.12	2.83 ± 3.23
$AAIW_3$	74 (1068)	65 (946)	93 (1343)	29 (422)
	0.38 ± 0.51	0.82 ± 0.68	0.09 ± 0.10	2.79 ± 3.30
$CDW_{1.6}$	93 (2281)	80 (1966)	52 (1284)	66 (1612)
	0.11 ± 0.10	0.26 ± 0.28	0.47 ± 0.55	0.24 ± 0.27
$NADW_{4.6}$	84 (1914)	80 (1815)	90 (2045)	70 (1594)
	0.29 ± 0.25	0.46 ± 0.42	0.12 ± 0.18	0.39 ± 0.50
$NADW_2$	95 (1698)	88 (1582)	44 (795)	78 (1390)
	0.21 ± 0.23	0.54 ± 0.46	0.67 ± 0.58	0.33 ± 0.43
$WSDW_{-0.3}$	90 (142)	82 (130)	88 (139)	89 (140)
	0.20 ± 0.06	0.54 ± 0.44	0.16 ± 0.11	0.14 ± 0.12
A17				
SMW_{27}	94 (96)	95 (97)	100 (102)	100 (102)
	0.14 ± 0.06	0.08 ± 0.07	0.02 ± 0.02	0.10 ± 0.04
$STMW_{18}$	68 (194)	84 (239)	90 (256)	66 (187)
	0.74 ± 0.34	0.39 ± 0.34	0.30 ± 0.31	0.51 ± 0.49
EQ_{13}	79 (1018)	81 (1037)	93 (1195)	38 (492)
	0.21 ± 0.17	0.21 ± 0.18	0.07 ± 0.10	0.77 ± 0.73
SACW-T_{18}	77 (201)	85 (223)	94 (245)	69 (180)
	0.92 ± 0.43	0.43 ± 0.37	0.37 ± 0.40	0.66 ± 0.77
$AAIW_5$	75 (1215)	67 (1085)	87 (1402)	37 (597)
	0.41 ± 0.42	0.85 ± 0.69	0.13 ± 0.19	3.16 ± 3.60
$AAIW_3$	68 (1344)	58 (1146)	82 (1617)	28 (558)
	0.33 ± 0.38	0.74 ± 0.64	0.13 ± 0.17	2.74 ± 3.59
$CDW_{1.6}$	89 (3544)	75 (2977)	60 (2408)	60 (2395)
	0.25 ± 0.31	0.45 ± 0.51	0.40 ± 0.48	0.34 ± 0.35
$NADW_{4.6}$	90 (2543)	85 (2412)	89 (2514)	70 (1973)
	0.26 ± 0.23	0.42 ± 0.41	0.14 ± 0.22	0.42 ± 0.52
$NADW_2$	91 (2914)	81 (2592)	57 (1822)	76 (2451)
	0.27 ± 0.24	0.50 ± 0.42	0.48 ± 0.49	0.31 ± 0.29
$WSDW_{-0.3}$	76 (918)	79 (950)	74 (895)	61 (734)
	0.33 ± 0.19	0.55 ± 0.40	0.15 ± 0.14	0.29 ± 0.24

$CDW_{1.6}$ and $NADW_2$ along WOCE line A14 and for $CDW_{1.6,}$ $NADW_2$ and $WSDW_{-0.3}$ along WOCE line A17 (Table 6).

3.5.4. Test 4: variability in the R_N ratio

R_N was varied between 9 and 12 at 0.1 unit intervals. NO values of the measurements and SWT were recalculated for each R_N and, then, the OMP analysis was run. A total of 31 solutions were obtained and the mean and standard deviation of the STD matrix (Section 3.5) for the SWT fractions obtained were calculated.

The reliability to reproduce the measured fields decreased, especially for the NO (Table 5). Interestingly, the mean *Total Residual* reduced in the upper 500 dbar and in the 2000–3000 dbar range compared to the best solution (Fig. 4). The stability of the mean solution after the R_N modifications was only reduced for the AAIW, but in general, the values were comparable to the best solution (Table 4). The water masses distribution along both lines was affected if the R_N is changed: most of the SWT presented a percentage of samples less than 80% equal to the best solution (Table 6).

3.5.5. Overview of the perturbation tests

The reliability of the perturbation tests was checked by comparing the determination coefficient and standard deviation of the residuals of the regression between the measured and predicted variables introduced in the OMP analysis. Table 5 shows that any of the OMP solutions predicted fairly well the distribution of the introduced variables. Perturbing the measured data 4-fold the typical measurement uncertainty was the test that produced a larger deviation of the *Total Residual* from the best solution. The test perturbing R_N seems to reproduce better the measured data compared to the best solution in some layers of the water column. In this case, a closer look at the *Individual Residuals* confirmed that the NO prediction improved in the R_N test; the positive bias in Fig. 3b around 3000 dbars disappeared and the *Individual Residuals* for NO distributed around cero (figure not shown).

The stability of the solutions was evaluated by examining the magnitude of the mean and standard deviation of the STD matrix for each SWT after the 100 (or 31) solutions per test. That is, being right or wrong, the SWT proportions given by the OMP solution can be more or less stable. Note that for any of the tests the mean or the standard deviation was less than 5% (Table 4).

The stability of the Central Waters was practically unaffected, but the Intermediate (AAIW) and Deep (NADW and CDW) Waters

presented differences depending on the test (Table 4). Particularly, perturbing the data and the SWT characteristics did have an impact in the stability of Intermediate and Deep Waters.

The former analyses point to the perturbation tests on the SWT characteristics and measured data as the main sources of error and instability in the OMP analysis. Remember that in both tests, SWT and measurements, the errors introduced were 4-fold greater than those typically considered.

Comparing the mean solution after the perturbation tests with our best solution, although somehow subjective, also gives valuable information (Table 6). Perturbing the R_N was the only test changing significantly the SWT distributions along both lines. In any case, it must be taken into account that even for the later test, the mean absolute differences for any SWT were less than 5% (see Appendix A).

In summary, changes in the weights has a minimum impact on the reliability and robustness of the OMP and the SWT distributions; SWT and data should be altered 4-fold their typical uncertainty to detect changes in the OMP best solution; and varying the R_N would be the main factor of uncertainty in our OMP best solution.

4. Distribution of water masses in the SAO

Water masses have been traditionally identified following extremes in physical and/or biogeochemical variables. For example, AAIW can be identified by a salinity minimum and NO, SiO_4 and oxygen maxima. Usually, these extremes do not coincide in depth, indicating that none of them matches with the core-of-flow of this water mass (Reid, 1989). The OMP analysis compiles the information provided by the extremes of all these variables to identify the realm and the core-of-flow of any water mass. The realm is defined as the region where the proportion of the water mass is >50% and the core-of-flow is defined as the depth of maximum proportion of the water mass.

In this section we will describe the distribution of the Central, Intermediate, Deep and Bottom Water masses identified with the OMP analysis, with special emphasis on the latitudinal evolution of the cores-of-flow. For the sake of simplicity, the vertical distributions of physical (potential temperature and salinity) and chemical (nitrate, phosphate, oxygen, NO, silicate and CFC-11) variables will not be presented. Note that they have been thoroughly described in Mémery et al. (2000) and Brea et al. (2004) for the WOCE lines A17 and A14, respectively (here included in Appendix B).

4.1. Central Waters

The vertical distribution of the sum of the 4 SWT modelling Central Waters in line A14 (SACW-E_{18}, SACW-E_{12}, SACW-T_{18} and SACW-T_{12}) are presented in Fig. 5a and the sum of the 4 SWT modelling the Central Waters in line A17 (SMW_{27}, $STMW_{18}$, SACW-T_{18} and EQ_{13}) in Fig. 6b. The bold lines correspond to the 50% contribution of each SWT.

Fig. 7 shows the meridional evolution of salinity, dissolved oxygen, SiO_4 and CFC-11 along the 13 °C isotherm in both WOCE lines. The depth of this isotherm (grey line in Figs. 5a and 6a) responded to the different wind regimes, fronts (Fig. 1) and biogeochemical provinces crossed by the two WOCE lines: equatorial, subequatorial, tropical, subtropical and subantarctic. Along line A14 (Fig. 5a), the abrupt rise in about 100 dbars of the 13 °C isotherm around 3°S marked the transition from the Equatorial Current System (ECS) to the SubEquatorial Gyre (SEG). South of 9°S, the isotherm sank gradually to ~250 dbar, reaching 300 dbar at 20–22°S, the limit between the SEG and the SubTropical Gyre (STG). Within

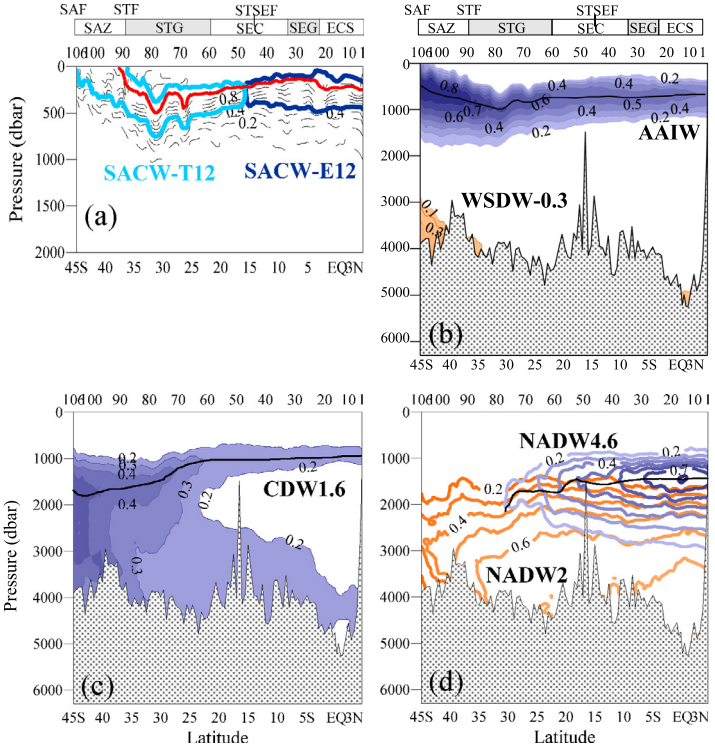

Fig. 5. Full-depth distributions of (a) Central Waters (sum of SACW-E_{18}, SACW-E_{12}, SACW-T_{18} and SACW-T_{12}) as dashed lines, the red line shows the 13 °C isotherm, (b) AAIW (sum of $AAIW_5$ and $AAIW_3$) and $WSDW_{-0.3}$, (c) $CDW_{1.6}$, and (d) $NADW_{4.6}$ and $NADW_2$ proportions along WOCE line A14. SAF, Subantarctic Front; SAZ, Subantarctic Zone; STF, Subtropical Front; STG, Subtropical Gyre; SEC, Subequatorial Current; STSEF, Subtropical–Subequatorial front; SEG, Subequatorial gyre; ECS, Equatorial Current System. The light blue bold line in (a) corresponds to the 50% contribution of SACW-T_{12} and the dark blue bold line the 50% contribution of SACW-E_{12}. Bold lines in (b), (c) and (d) show the maximum of AAIW, $CDW_{1.6}$ and $NADW_{4.6}$, respectively. (For interpretation of the references to colour in this figure legend, the reader is referred to the web version of this article.)

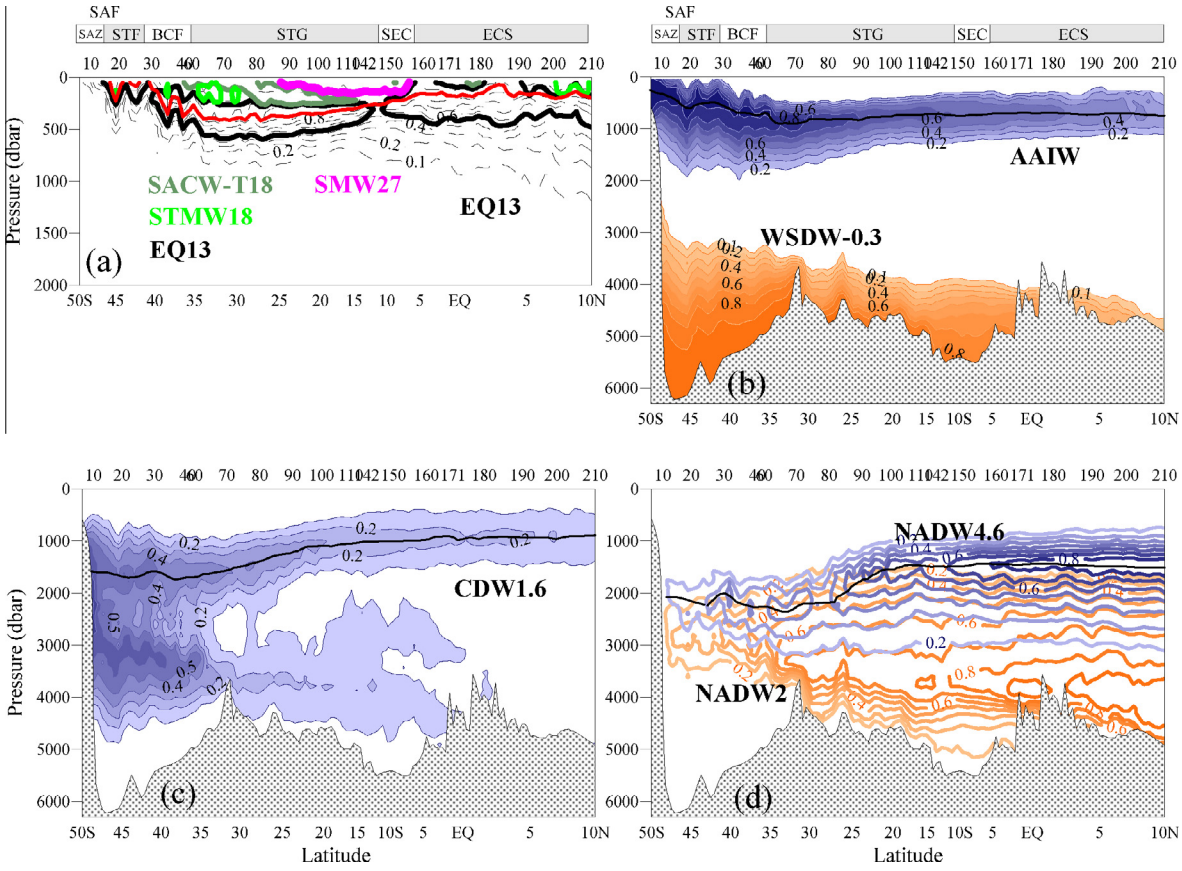

Fig. 6. Full-depth distributions of (a) Central Waters (sum of SMW_{27}, $STMW_{18}$, $SACW\text{-}T_{18}$ and EQ_{13}) as dashed lines, the red line shows the 13 °C isotherm, (b) AAIW (sum of $AAIW_5$ and $AAIW_3$) and $WSDW_{-0.3}$, (c) $CDW_{1.6}$, and (d) $NADW_{4.6}$ and $NADW_2$ proportions along WOCE line A17. SAF, Subantarctic Front; SAZ, Subantarctic Zone; STF, Subtropical Front; STG, Subtropical Gyre; SEC, Subequatorial Current; STSEF, Subtropical–Subequatorial front; SEG, Subequatorial gyre; ECS, Equatorial Current System. The black bold line in (a) corresponds to the 50% contribution of EQ_{13}, the light green bold line to 50% $STMW_{18}$, and the dark green bold line to 50% $SACW\text{-}T_{18}$; the pink bold line to 50% SMW_{27}. Bold lines in (b), (c) and (d) show the maximum of AAIW, $CDW_{1.6}$ and $NADW_{4.6}$, respectively. (For interpretation of the references to colour in this figure legend, the reader is referred to the web version of this article.)

the STG, two anticyclonic eddies were detected where the 13 °C isotherm abruptly sank to more than 500 dbar. These eddies were detached from the Agulhas Current System, carrying warmer and more saline Indian waters into the SAO (Arhan et al., 1998). The SubTropical Front (STF) was detected by a steep decrease in depth of the 13 °C isotherm. South of this front, Central Waters are colder than 13 °C and we entered the SubAntarctic Zone (SAZ).

Along line A17, the Equatorial Current System (ECS) was identified by the constant depth of the 13 °C isotherm at ~170 dbar north of 5°S (Fig. 6a). Vertical excursions of the isotherm around 3°N and 8°N corresponded to the North Equatorial UnderCurrent (NEUC) and the North Equatorial CounterCurrent (NECC), also noted in the distribution of the chemical variables (see below). The westward-flowing SouthEquatorial Current (SEC) was marked by the rise of the 13 °C isotherm between 16°S and 5°S. Within the STG, the isotherm remained around 400 dbar. Line A17 crossed 5 times the Brazil Current Front (BCF) between 34°S and 40°S, as this current detaches from the continental slope in this latitudinal range (Olson et al., 1988; Peterson and Stramma, 1991). The BCF is indicated by the 10 °C isotherm at 400 m depth (Roden, 1986). Further south, the STF was crossed 5 times between 46°S and 41°S, as indicated when the 10 °C isotherm is at 100 m depth (Mémery et al., 2000). The region between 52°S and 39°S presented a complex circulation; it is the confluence region of the southward flowing Brazil Current (BC) and the northward flowing Malvinas Current (MC) (Fig. 1) where eddies are frequently formed. Two anticyclonic eddies were detected around 45.5°S and 43°S (Fig. 6a) detached from the Brazil Current. The Malvinas Front (MF) or SubAntarctic Front (SAF) located around 48°S, where the 13 °C isotherm rose to 100 dbar. South of the MF colder and less saline waters were encountered.

The meridional evolution of the physical and chemical characteristics of the 13 °C isotherm are shown in Fig. 7. In the northern end of both WOCE lines, salinity was very similar; higher values were found in line A17 within the subtropical gyre, as higher evaporation rates were reported for the western SAO (Gordon and Bosley, 1991). Along line A14, the Agulhas eddy around 27°S was clearly detected while no signal was seen for the one at 31°S; south of the STF, at ~37°S, salinity steeply decreased as the line entered the SAZ. Along line A17, salinities were high north of 5°N, associated with the NECC, while the rest of the ECS from 10°S to 5°N had a nearly constant salinity; the subtropical gyre was characterized by a bowl shape salinity distribution. The northward increase between 10°S and 5°S indicated the position of the SEC. South of 37°S the up and downs of salinity marked the MC–BC confluence and the MF appeared as a steep decrease southwards, around 48°S.

Along line A14, the chemical characteristics, especially oxygen and CFC-11, clearly identified the STF at ~37°S and the transition from subtropical to subequatorial waters at ~15°S (Fig. 7b–d). This transition was also well defined along line A17 in oxygen, silicate and CFC-11. The NECC, associated with high salinities, presented a prominent signal of high silicate but low oxygen and CFC-11, indicating lower ventilation. The waters in the ECS from 5°S to 5°N were characterized by relative maxima of oxygen and CFC-11. The MC–BC confluence region was indicated as spikes in the chemical distributions south of 40°S.

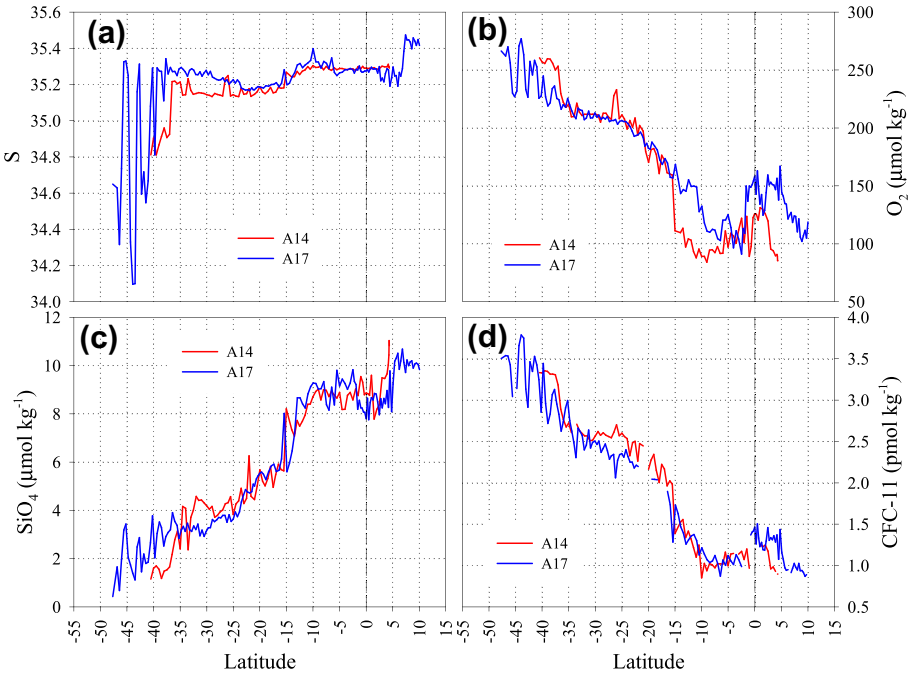

Fig. 7. Meridional evolution along lines A14 and A17 of (a) salinity (*S*, psu), (b) oxygen (O_2, µmol kg^{-1}), (c) silicate (SiO_4, µmol kg^{-1}) and, (d) CFC-11 (pmol kg^{-1}) along the 13 °C isotherm.

Within the subequatorial region, the upper 500 dbar of line A14 was occupied by SACW-E_{12} (Fig. 5a). Within the subtropical gyre, from 15°S to 37°S, the subtropical variety of SACW with lower salinities and silicate, higher oxygen and CFC-11 (Fig. 7) was the dominant water mass from 200 down to about 500 dbar. Deeper excursions corresponded to the Agulhas Current eddies (Fig. 5a). Within this region, the upper 200 dbar was occupied by the warmer SACW-T_{18}.

The distribution of Central Waters along line A17 was more complex (Fig. 6a). Within the ECS, north of 10°S the main water mass from 100 to 400 dbar was EQ_{13}, fed into the NBC from its source area in the eastern SAO; within the SEC SMW_{27} occupied the upper 150 dbar, the northern limit of its maximum contribution marked the South Equatorial CounterCurrent (SECC) intersection with the WOCE line (Mémery et al., 2000). Along line A17 and according to Mémery et al. (2000) the southern limit of SMW_{27} was established where salinities lower than 36 were detected at the surface (28–30°S), from the OMP analysis the SMW_{27} southern limit would be around 23°S where the less saline SACW-T_{18} contributed with more than 50% (Fig. 6a). Between 28°S and 23°S, SACW-T_{18} occupied the upper 250 dbar subducting under the SMW_{27}. North of the STF between 40°S and 32°S, the warmer and more saline $STMW_{18}$ occupied the upper 200 dbar. The 28°S front commented by Mémery et al. (2000) as the limit of the Brazil Current recirculation separating subtropical from tropical waters is here marked by the southward rise of the 50% SACW-T_{18} contribution. In the subtropical region between 250 and 500 dbar EQ_{13} dominated; it should be carried to the western SAO by the Brazil Current recirculations and the SEC. EQ_{13} shallowed southwards disappearing south of the MF.

4.2. Antarctic Intermediate Water (AAIW)

The AAIW results will be presented as the sum of the two SWT representing this water mass: $AAIW_{3.1}$ and $AAIW_5$. Traditionally, AAIW has been identified as a salinity minimum at intermediate depths or a local oxygen maximum, somewhat shallower than the salinity minimum (e.g., Peterson and Whitworth, 1989; Piola and Gordon, 1989; Suga and Talley, 1995). The salinity minimum was detected all along both sections although the oxygen maximum gradually vanished between 24°S and 14°S in line A17 and between 20°S and 25°S in line A14 (see Appendix B), due to the oxygen minimum associated with Central Waters in the subtropical-subequatorial transition. AAIW formed in the MC–BC confluence region followed the subtropical and subequatorial gyre circulation (Larqué et al., 1997; Warner and Weiss, 1992). This complex circulation directly affected the meridional distribution of chemical variables along the core-of-flow of AAIW (Figs. 5b, 6b) in both WOCE lines (Fig. 8).

The highest proportions of AAIW (>90%) were found at ~500 dbar in the southern end of line A17, where it forms (Fig. 6b). North of the STF, AAIW subducted to ~1000 dbar and it ascended to about 800 dbar in the SEC, keeping this depth for the rest of the section. The same distribution was observed along line A14 (Fig. 5b), but with lower proportions (~80%) to the south given that AAIW dilutes when transported from line A17 to line A14 by the South Atlantic Current (SAC).

The meridional evolution of salinity along the core-of-flow of AAIW (Fig. 8a) was controlled by the different regimes crossed by this water mass: salinity gradients were major where mixing was the dominant physical process as within the subtropical gyre (from 35°S to 20°S), but minor where advection was dominant as within the SEC (around 15°S). A salinity gradient was not found in the subequatorial gyre along line A14 (~5°S). Therefore the AAIW flowing northwestwards within the SEC had practically the same salinity as the AAIW carried by the South Intermediate CouterCurrent (SICC). North of the Equator, salinity increased in both WOCE lines because the AAIW reaching the western basin with the SEC (i) deviated northwards within the North Brazil Current (NBC) crossing the Equator; (ii) where it mixed with the more salty Central Waters of the North Atlantic waters; and (iii) returned eastwards with the North Intermediate CounterCurrent (NICC). Therefore, the AAIW transported by the SICC and NICC had different salinities.

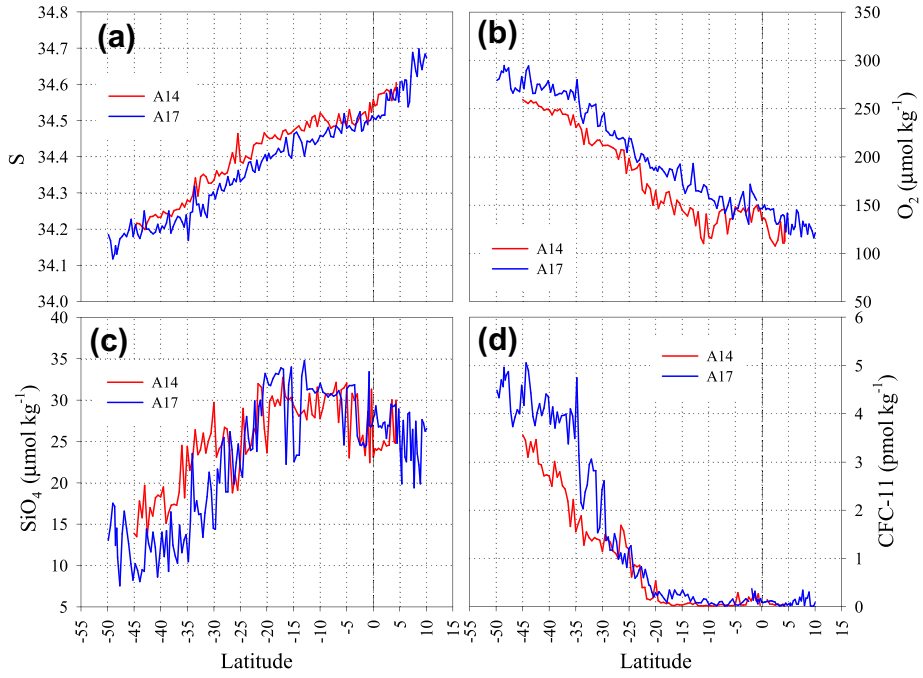

Fig. 8. Meridional evolution of (a) salinity (*S*, psu), (b) oxygen (O_2, µmol kg^{-1}), (c) silicate (SiO_4, µmol kg^{-1}) and, (d) CFC-11 (pmol kg^{-1}) in the level of maximum proportion of AAIW (defined as $AAIW_{3.1}$ + $AAIW_5$) along lines A14 and A17.

Oxygen along the core-of-flow of AAIW (Fig. 8b) decreased northwards. At 35°S, around the STF, oxygen sharply decreased in both WOCE lines. Along line A14, another sharp decrease around 23°S marked the transition from southern (younger) waters to northern (older) waters within the subequatorial gyre. Along line A17, oxygen remained constant within the SouthEquatorial Current System, decreasing north of the Equator. This is because AAIW carried within SICC is younger than that in the NICC, as it has covered a longer distance from its formation area. The meridional evolution of silicate was noisier than salinity or oxygen (Fig. 8c). In general it increased northwards in both WOCE lines. The two eddies at 26°S and 24°S along line A14 were detectable by a sharp decrease of silicate. Maxima silicate values were reached at the SEC in both WOCE lines and also within the subequatorial gyre in line A14. Silicate decreased at the Equator to increase further north. As expected, CFC-11 concentrations (Fig. 8d) were higher in line A17, decreasing northwards until about 20°S where they reach undetectable levels in both WOCE lines.

4.3. Circumpolar Deep Water (CDW)

The mixing of Deep Waters from the major oceans in the Antarctic Circumpolar Current produces large volumes of CDW, characterized by an oxygen minimum and nutrients maxima. This water mass locates underneath AAIW and shrinks northwards as it encounters the southward flowing NADW at the same density ranges (Figs. 5 and 6). NADW divides CDW in two well separated parts, the Upper Circumpolar Deep Water (UCDW), characterized by an oxygen minimum and nutrient maximum, overriding NADW and the lower part (LCDW), characterized by a weak salinity maximum, underneath NADW, that it is generally considered part of AAWB (Whitworth and Nowlin, 1987; Tsuchiya et al., 1994).

Along both lines, the UCDW can be followed by the nitrate maximum (see Appendix B) although only until 23°S. North of that latitude this maximum merges with the salinity minimum associated with AAIW. UCDW can also be identified by an oxygen minimum and a silicate maximum (see Appendix B). The oxygen minimum located about 200 dbar underneath the nitrate maximum was not detected north of 23°S. However, the silicate maximum, located 200 dbar deeper than the oxygen minimum, can be traced all along both WOCE lines, leading some authors to conclude that the UCDW extends north of 23°S (McCartney, 1993; Oudot et al., 1998; Andrié et al., 1998).

Along line A17, Mémery et al. (2000) studied in detail the confluence between UCDW (identified by an oxygen minimum) and NADW (identified by a salinity maximum) in the $36.8 < \sigma_2 < 36.85$ range. They met at 26°S, where the UCDW oxygen minimum sharply shifted to densities lower than 32.2 σ_1 northwards and the NADW salinity maximum to densities higher than 36.95 σ_2 northwards. Looking at the meridional distributions of silicate and CFC-11 along the 36.9 σ_2 isoline, they identified again 26°S as the juxtaposition of UCDW and NADW in the SAO. The westward flow of UCDW within the northern limb of the subtropical gyre is found at 26–30°S (Reid, 1989), while the eastward turning of NADW occurs at 20–25°S related with the presence of the Vitoria-Trinidade Ridge (Hogg and Owens, 1999). According to Mémery et al. (2000), the intermittent oxygen minima below 800 dbar detected along the line A17 north of 26°S are ascribed to the uppermost portion of UCDW, even reaching the equatorial domain carried within the NBUC.

The quantitative analysis performed here allowed us to go a step forward: the northward shoaling of the core-of-flow of UCDW and the steep decrease in its contribution was detected on both WOCE lines around 26°S (Figs. 5c and 6c). North of this latitude the maximum contribution of UCDW was less than 30% and the core rises from about 1900 to 1000 dbar. The contribution reduced to less than 20% within the equatorial region. Note that north of 26°S the dominant water mass was AAIW (Figs. 5b and 6b). If we follow the UCDW maximum contribution along both WOCE lines (figure not shown) around 26°S there was a sharp northward decrease from 35% to less than 30%, and north of the Equator, around 20%. As previously commented, AAIW was the main contributor (40–50%) and, consequently, the silicate maximum associated with UCDW by some authors actually corresponded to AAIW as also

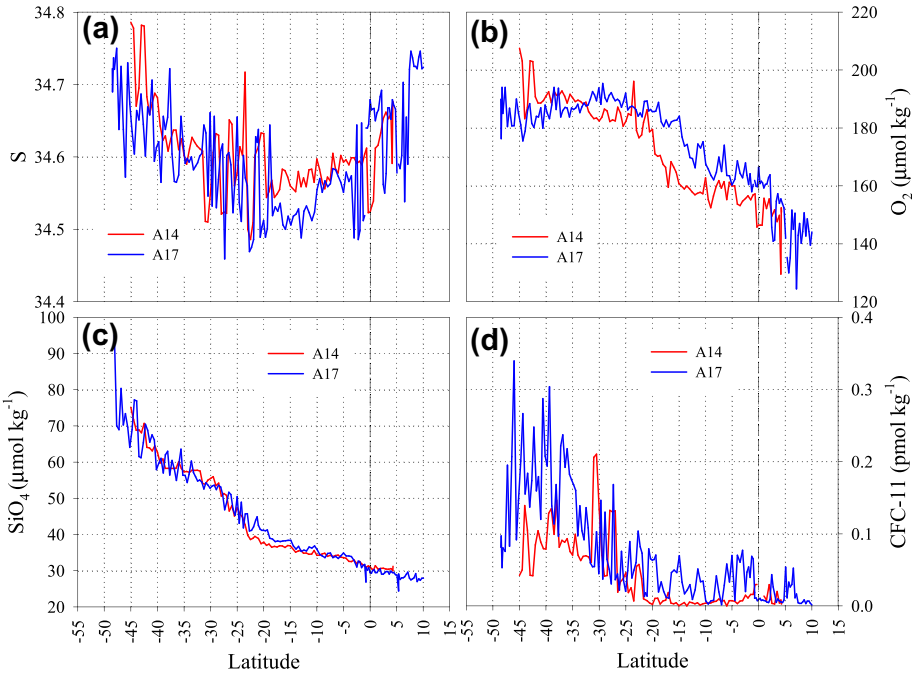

Fig. 9. Meridional evolution of (a) salinity (*S*, psu), (b) oxygen (O_2, µmol kg^{-1}), (c) silicate (SiO_4, µmol kg^{-1}) and, (d) CFC-11 (pmol kg^{-1}) in the level of maximum proportion of $CDW_{1.6}$ along lines A14 and A17.

pointed by Tsuchiya et al. (1994). Therefore, our water mass analysis has helped to solve the controversy between AAIW and UCDW: north of 23°S AAIW is the dominant water mass at the UCDW maximum, which reached the equatorial area in a proportion of 20% and explained the intermittent oxygen minima reported by Mémery et al. (2000) north of the Equator.

Fig. 9 shows the distribution of salinity and chemical variables along the UCDW maximum (Figs. 5c and 6c) in both lines. The meridional distribution of salinity (Fig. 9a) was not as uniform as along the AAIW maximum (Fig. 8a). In general, salinity decreased within the subtropical gyre, increased in the SEC and increased again in the ECS, north of the Equator it increases again. Along line A14, the two eddies at 26°S and 31°S were clearly marked. In general, oxygen (Fig. 9b) decreased northwards with higher values along line A17, as CDW is transported to the eastern SAO within the Subtropical Current; the sharpest oxygen decrease occurred at 15°S in line A17 and at 30°S in line A14. Therefore, it seems that oxygen is not a proper tracer to detect the confluence of UCDW and

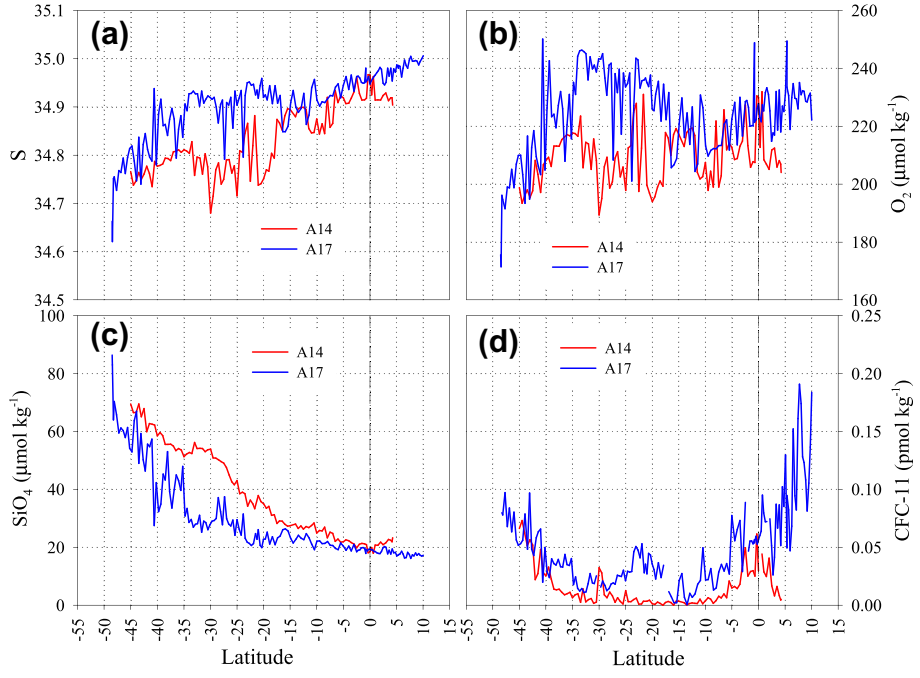

Fig. 10. Meridional evolution of (a) salinity (*S*, psu), (b) oxygen (O_2, µmol kg^{-1}), (c) silicate (SiO_4, µmol kg^{-1}) and, (d) CFC-11 (pmol kg^{-1}) in the level maximum proportion of $NADW_{4.6}$ along lines A14 and A17.

NADW, as both water masses do not have such a contrasting oxygen concentration. On the contrary, silicate (Fig. 9c) marked this transition very well, with a sharp northwards decrease at 23°S on both sections. CFC-11 concentrations at the UCDW maximum were an order of magnitude lower than at the AAIW maximum (Figs. 8d and 9d). As expected, the concentration of CFC-11 was lower along line A14 than along line A17. The two eddies along line A14 were clearly marked also in the distribution of this tracer.

4.4. North Atlantic Deep Water (NADW)

Upper NADW is characterized by salinity maxima and silicate minima, due to the Mediterranean Water influence. These extremes are located around 1600 dbar in the western SAO. Middle NADW, with a Labrador Sea Water influence, is characterized by a nitrate minimum and an oxygen maximum situated around 2000–2200 dbar. The deepest component, Lower NADW, with influence from the North Atlantic overflows, is characterized by a second nitrate minimum and oxygen maximum around 3800 dbar. Except for the LNADW along line A14, the former extremes can be identified in both WOCE lines (see Appendix B).

Briefly, along line A14, NADW was identified within the 1700–2200 dbar range by salinity (>35) and oxygen (>240 μmol kg^{-1}) maxima and silicate minimum (<20 μmol kg^{-1}) (see Appendix B). This is a small fraction of the southward flowing NADW entering the SAO within the DWBC that deflects eastward along the Equator (Weiss et al., 1985). The extremes identifying UNADW and MNADW can be detected along line A14: for the UNADW a salinity maximum (1700–1800 dbar) and silicate minimum (1600–1700 dbar); for the MNADW a nitrate minimum (1900–2000 dbar) and oxygen maximum (2000–2200 dbar). The deepest component, LNADW, flows at deeper levels than the Mid Atlantic Ridge depth in the eastern SAO. LNADW enters the eastern SAO diluted with AABW which also crosses eastward through the Romanche and Chain Fracture Zones (Mercier and Morin, 1997; Ferron et al., 1998; Mercier and Speer, 1998). Therefore, it reaches 9°W very diluted and their characteristic extremes cannot be identified.

Along line A17, the extremes related with UNADW appeared at 1600–1800 dbar between 10°N and 21°S, but deepened to 2400–2600 dbar from 21°S to 26°S (see Appendix B). Within the former latitudinal band, UNADW deflected eastward from the continental slope of South America (Reid, 1989; Tsuchiya et al., 1994; Durrieu De Madron and Weatherly, 1994) as it encountered the northward flowing UCDW. The oxygen maximum/nitrate minimum associated with MNADW followed the salinity maximum but about 200 dbar deeper. The second oxygen maximum (related with a nitrate and silicate minimum) associated with LNADW located around 3800 dbar. A somewhat shallower NO minimum also identified LNADW. This water got shallower towards the south as it encountered the densest WSDW flowing northwards within the Brazil basin. Within the latitudinal band 21–26°S, as previously commented, UCDW encountered NADW. The shallowest components, UNADW and MNADW, converged into LNADW. In fact, south of 26°S there was only one NO minimum and south of 32°S the

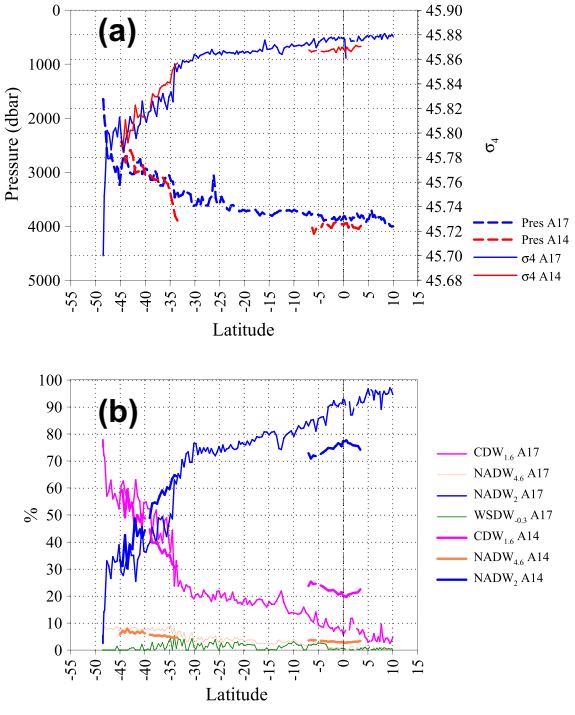

Fig. 11. Meridional evolution of (a) pressure (dbar) and density σ_4 along the 2 °C isotherm and, (b) fractions (in percentages) of $CDW_{1.6}$, $NADW_{4.6}$, $NADW_2$ and $WSDW_{-0.3}$ for the same isotherm along lines A14 and A17.

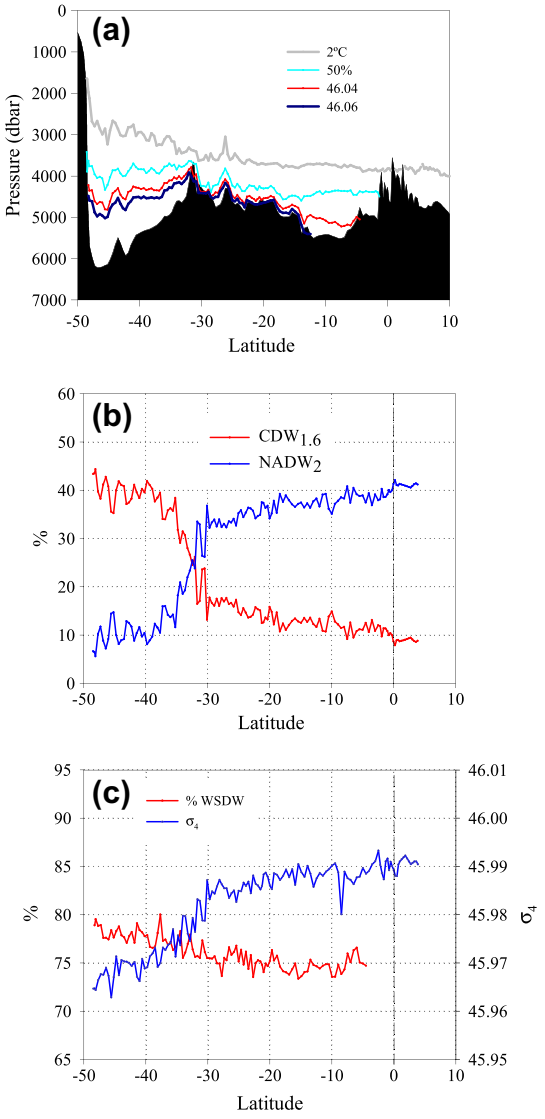

Fig. 12. Meridional evolution along line A17 line of (a) the 2 °C isotherm, the 50% contribution of $WSDW_{-0.3}$, and the σ_4 46.04 and 46.06 levels; (b) the fractions of $CDW_{1.6}$, and $NADW_2$ along the 50% $WSDW_{-0.3}$ layer (in percentages) and; (c) the $WSDW_{-0.3}$ fraction (in percentages) along the σ_4 46.04 isoline and σ_4 along the 50% $WSDW_{-0.3}$ layer.

salinity maximum/silicate & nitrate minimum converged. So, there was just one NADW nucleus. Around 26°S, in addition to the UCDW entry, WSDW shoaled, contributing to the convergence of the three NADW components. This shoaling of the WSDW seems to be related with the topography: a seamount north of the Rio Grande Rise is located around 26°S inducing a deep cyclonic eddy associated with the NADW eastward return flow (Arhan et al., 2002).

The distribution of the $NADW_{4.6}$ (representative for the UNADW and MNADW) and $NADW_2$ (representative for the LNADW) are shown in Figs. 5d and 6d for lines A14 and A17, respectively. Along line A17 (Fig. 6d), the highest contributions (>90%) of both NADW components were found towards the northern end of the line. The $NADW_{4.6}$ maximum located around 1500 dbar until 23°S where it deepened until 2400 dbar at 35°S, from 45°S it began to shoal until reaching 1700 dbar at the southern end of the line. The $NADW_2$ maximum located at 4100 dbar at the northern end of the line, uplifted to 3900 dbar at 7°N, remained there until 10°S and began to shoal from 30°S, reaching 2000 dbar at the southern end of the section. These distributions perfectly corresponded with the general knowledge about NADW circulation in the SAO (e.g., Stramma and England, 1999) and the findings about the eastward escapes of NADW from line A17 described by Mémery et al. (2000).

Maximum contributions (>90%) of $NADW_{4.6}$ along line A14 (Fig. 5d) were found around the Equator. The $NADW_{4.6}$ maximum remained around 2000 dbar until 23°S where it sharply deepened to 3000 dbar where it merged with $NADW_2$ and CDW coming from the west (Arhan et al., 2002). South of 40°S, the level of maximum proportion of NADW was composed of ~40% of NADW and ~60% of CDW (Fig. 5e and d).

In the case of line A17, if we follow the $NADW_{4.6}$ maximum (figure not shown but see Fig. 6), a sharp decrease occurred at 26°S and south of 37°S the contribution of CDW was higher than the $NADW_{4.6}$ or $NADW_2$ contributions; the maximum contribution of $NADW_2$ continuously increased southwards, with a maximum (40%) at 28°S; from here it decreased in parallel with $NADW_{4.6}$. Along the $NADW_2$ maximum, a sharp decrease from >70% to

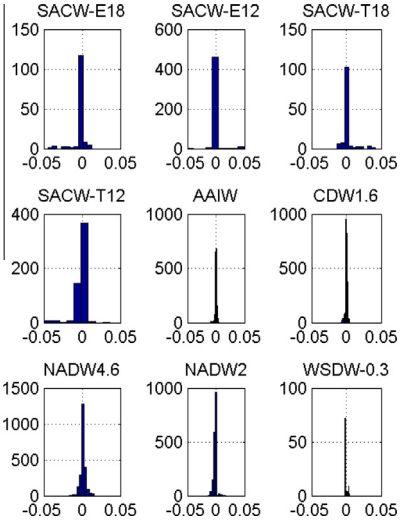

Fig. A1. WOCE line A14. Variability in the SWT properties. Histograms showing the distribution of the difference between the perturbed and best solution mean SWT fractions. AAIW represents $AAIW_5$ + $AAIW_3$.

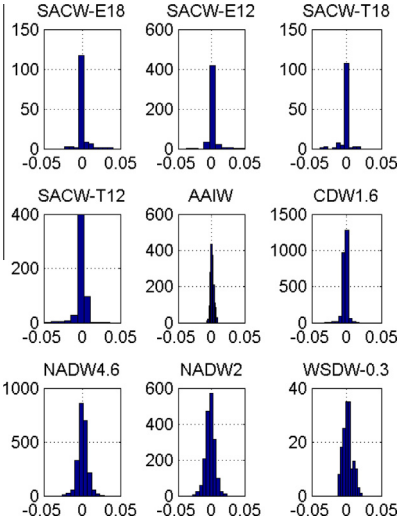

Fig. A3. WOCE line A14. Variability in the measured variables. Histograms showing the distribution of the difference between the perturbed and best solution mean SWT fractions. AAIW represents $AAIW_5$ + $AAIW_3$.

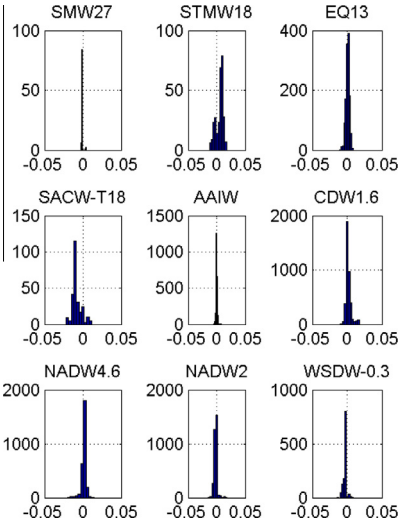

Fig. A2. WOCE line A17. Variability in the SWT properties. Histograms showing the distribution of the difference between the perturbed and best solution mean SWT fractions. AAIW represents $AAIW_5$ + $AAIW_3$.

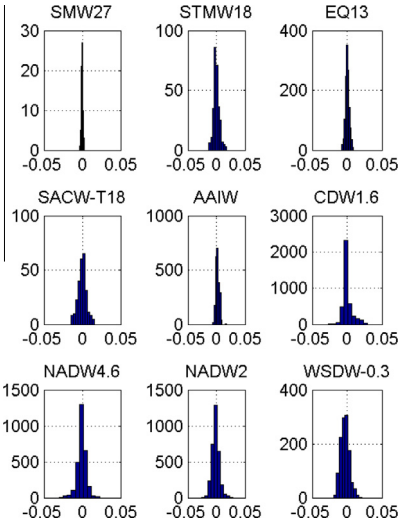

Fig. A4. WOCE line A17. Variability in the measured variables. Histograms showing the distribution of the difference between the perturbed and best solution mean SWT fractions. AAIW represents $AAIW_5$ + $AAIW_3$.

<50% occurred at 32°S, and south of 40°S, the deepest CDW was the highest contributor (>40%).

The distribution of salinity, oxygen, silicate and CFC-11 along the $NADW_{4.6}$ maximum in the eastern and western SAO (Fig. 10) marked again the circulation and mixing patterns of this water mass within the SAO. Along line A17, salinity (Fig. 10a) continuously decreased until 15°S where the $NADW_{4.6}$ contribution reduced to <70% (Fig. 6d); from here it rose and abruptly decreased south of 35°S, where $NADW_{4.6}$ directly encountered CDW (Fig. 6). The oxygen evolution (Fig. 10b) was parallel to that of salinity; salinity and oxygen increased between 20°S and 30°S related with a higher contribution of $NADW_2$ (Fig. 6) along this maximum. $NADW_2$ has practically the same salinity as $NADW_{4.6}$ (Table 2) and is identified with an oxygen maximum. Silicate (Fig. 10c) kept around 20 μmol kg^{-1} until a sharp rise to values >40 μmol kg^{-1} south of 35°S. A spike in silicate occurred around 26°S where the $NADW_2$ isoline rose to shallower depths (Fig. 6d) due to a deep cyclonic eddy. CFC-11 (Fig. 10d) presented a bowl shape distribution with higher values at the northern end of the line because it was near the source region (i.e. it was younger) and at the southern end of the line because it mixed with Lower CDW (Fig. 6). The spike in CFC-11 within 20–25°S (Fig. 10d) seemed to be related with the encounter with UCDW (Fig. 6).

Along line A14 in the $NADW_{4.6}$ maximum, salinity (Fig. 10a) decreased southwards, with a minimum at ~20°S, where the contribution of $CDW_{1.6}$ sharply increased to 30%, also producing a minimum in the oxygen evolution (Fig. 10b). Silicate (Fig. 10c) increased southwards with higher values in this line compared to line A17, because CDW (higher in silicate, Table 2) contributed more to the $NADW_{4.6}$ maximum in the eastern SAO. The same reason explains the lower values of CFC-11 (Fig. 10d) along this line.

4.5. Antarctic Bottom Water (AABW)

Within the SAO, AABW is formed from two main water masses: WSDW, very cold and dense ($\theta < 0$ °C, $\sigma_4 > 46.07$) and LCDW, less

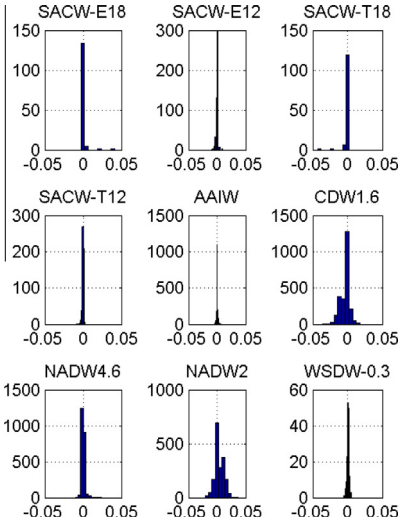

Fig. A5. WOCE line A14. Variability in the weights. Histograms showing the distribution of the difference between the perturbed and best solution mean SWT fractions. AAIW represents $AAIW_5$ + $AAIW_3$.

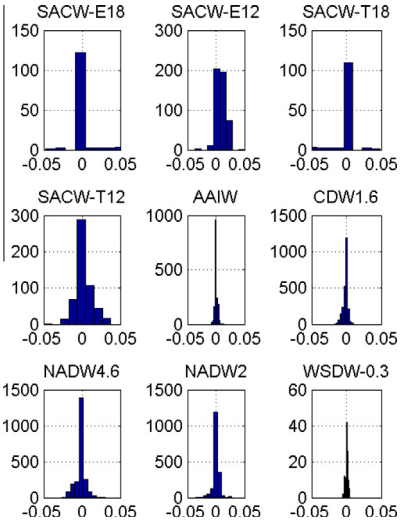

Fig. A7. WOCE line A14. Variability in the R_N ratio. Histograms showing the distribution of the difference between the perturbed and best solution mean SWT fractions. AAIW represents $AAIW_5$ + $AAIW_3$.

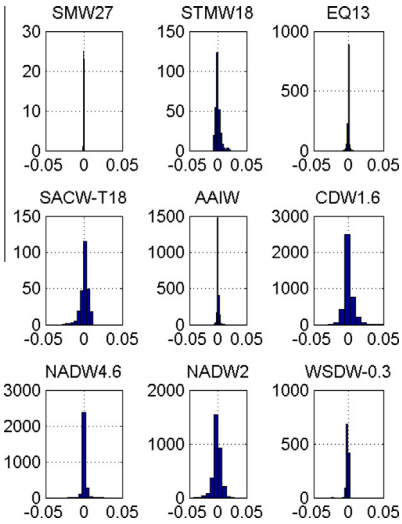

Fig. A6. WOCE line A17. Variability in the weights. Histograms showing the distribution of the difference between the perturbed and best solution mean SWT fractions. AAIW represents $AAIW_5$ + $AAIW_3$.

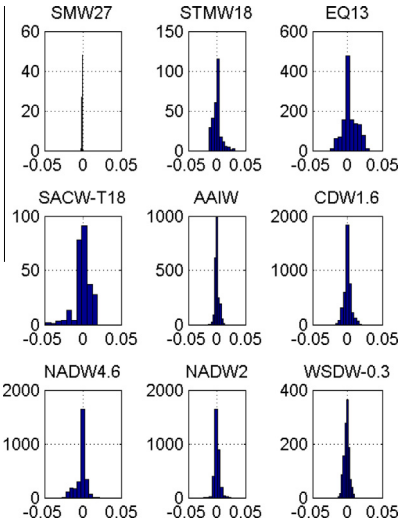

Fig. A8. WOCE line A17. Variability in the R_N ratio. Histograms showing the distribution of the difference between the perturbed and best solution mean SWT fractions. AAIW represents $AAIW_5$ + $AAIW_3$.

dense and warmer ($0 < \theta < 2$ °C, $45.85 < \sigma_4 < 46.07$), that flows within the ACC and enters the SAO from the Pacific through the Drake Passage (Reid, 1989; Arhan et al., 1998). AABW is located between the NADW and the bottom, and is detected as a sharp change in the relation between salinity and potential temperature (the Two Degree Discontinuity, TDD), and a sudden increase in silicate around the 2 °C isotherm. The high silicate concentration in WSDW derives from its formation in contact with rich opal sediments in the Weddell Sea platform (Edmond et al., 1979).

WSDW describes a large C-shaped cyclonic pattern in the southwestern corner of the Argentine Basin, and an anticyclonic flow around the Zapiola Ridge. Part of the WSDW entering the Argentine Basin flows along the Falkland Escarpment in the cyclonic circulation, another vein goes northward, feeding the flow around the Zapiola Ridge (Coles et al., 1996; Smythe-Wright and Boswell, 1998). Bottom maxima of CFC-11 and oxygen at the southern end of line A17 confirmed this scheme (Mémery et al., 2000).

Towards the north, WSDW crosses the Vema Channel around 31°S and flows northward as a narrow band confined west of 28°W in the Brazil Basin (McCartney and Curry, 1993; Durrieu De Madron and Weatherly, 1994). Within this basin, LCDW and WSDW mix so vigorously that the extremes identifying LCDW (salinity maximum and nutrient minima) disappear (Durrieu De Madron and Weatherly, 1994; Larqué et al., 1997). The core of pure LCDW is deviated towards the east as it has the same density as LNADW flowing southwards within the continental slope and also forced by WSDW flowing northwards west of 28°W (McCartney and Curry, 1993).

WSDW enters the Cape Basin from the south and a small amount of the warmest component goes through the Walvis Ridge into the Angola Basin (Connary and Ewing, 1974). A high silicate signal associated with AABW is detected in the Sierra Leone Basin, as this water crosses eastward through the Romanche and Walvis Passage (Onken, 1995; Mercier and Morin, 1997).

AABW can be perfectly detected, but not quantified, from the physical and chemical distributions (see Appendix B) along lines A17 and A14. Along line A14, AABW was found south of 32°S, where the 2 °C isotherm reached the bottom, and around 3°S, where this isotherm appeared again. Silicate also pointed the occurrence of AABW, with values >84 μmol kg^{-1} at 45°S and >50 μmol kg^{-1} at the Equator. In the western SAO, the 2 °C isotherm was detected all along line A17, at around 3000 dbar in the Argentine Basin and at around 3500 dbar north of the Vema Channel (32°S). Within the Argentine Basin, AABW was also detected by a sharp increase in silicate and nitrate towards the bottom, while oxygen and NO were quite homogeneous. Within the Brazil Basin, AABW mixed with NADW and the silicate concentrations decreased. North of 1°S, the Equatorial Channel, 4500 m deep, bars the flow to the Guyana Basin of the coldest AABW, but the high silicate, nitrate and NO and low oxygen signals were detected till the northern end of line a17.

The OMP results for WSDW along the two WOCE lines (Figs. 5b and 6b) are in complete agreement with the circulation patterns previously commented. Along line A14 (Fig. 5b) WSDW was found south of 35°S with contributions <40%, while north of the Equator, the contributions reduced to <10%. Along line A17, abyssal waters, >5000 dbar, within the Argentine Basin contained >90% of WSDW

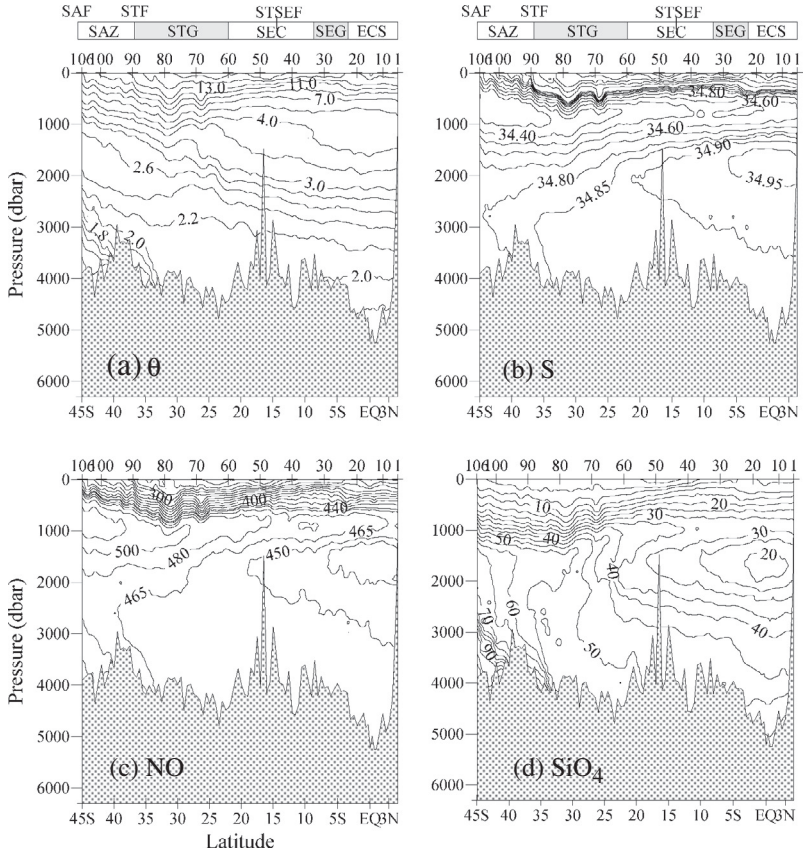

Fig. B1. Full-depth distributions of (a) potential temperature (θ, °C), (b) salinity (S, psu), (c) NO (μmol kg^{-1}) and (d) silicate (SiO4, μmol kg^{-1}) along WOCE line A14. SAF, Subantarctic Front; SAZ, Subantarctic Zone; STF, Subtropical Front; STG, Subtropical Gyre; SEC, Subequatorial Current; STSEF, Subtropical–Subequatorial front; SEG, Subequatorial gyre; ECS, Equatorial Current System.

(Fig. 6b). The contribution decreased towards the north, reaching 10% at 10°N. The cascading of the isolines at the Vema Channel and the deep cyclonic eddy at 26°S were clearly seen.

4.5.1. The Two Degree Discontinuity (TDD)

One way to follow the AABW circulation is based on the change of slope in the θ–S diagram at 2 °C, separating warmer waters with a North Atlantic influence from colder waters with an Antarctic influence. This is the Two Degree Discontinuity (TDD) defined by Broecker et al. (1976). According to this definition, any deep water colder than 2 °C is considered as AABW.

Fig. 11 shows the meridional evolution of the 2 °C isotherm pressure (dbar) and density (σ_4) and the contribution of the different water masses to this isotherm. Along line A17, the 2 °C isotherm abruptly deepened (Fig. 11a) in the MC–BC confluence region; north of 35°S the pressure increase was more progressive until 20°S where it reached 3700 dbar, it kept there until the Equatorial Current System where it deepened slightly. At 26°S there was a spike in the isotherm related with the submarine seamount north of the Rio Grande Rise. Density increased sharply in the confluence region and then until 35°S, the Vema Channel, northwards it steadily increased until 45.88 σ_4 at the northern end of the line. AABW enters from the ACC into the eastern SAO where it flows northwards within the Cape Basin. At these latitudes it presented the same pressure and density evolution as along line A17 (Fig. 11a). The Walvis Rise stopped AABW to flow northward: the AABW encountered at the Equator in the eastern SAO comes from the western SAO crossing the Romanche and Chain Fractures. It has travelled a long way across the SAO and it presents a lower density but it is found slightly deeper than AABW in line A17.

The TDD can be considered as the upper limit of AABW: the meridional evolution of the SWT fractions along the TDD (Fig. 11b) revealed that WSDW and $NADW_{4.6}$ contribute less than 5% and 10% along lines A14 and A17, respectively. In the western SAO the main contributor south of the Vema Channel (35°S) was CDW and north of it $NADW_2$. In the eastern SAO, the main contributor south of the Walvis Ridge (39°S) was CDW and $NADW_2$ northwards.

4.5.2. The 46.06 σ_4 and the 50% WSDW isolines

The classical approach to study the WSDW spreading in the SAO is by following the 46.06 σ_4 isoline (e.g., Reid, 1989) given that this is the maximum density of deep Pacific waters entering the SAO through the Drake Passage. Therefore, denser waters would have a Weddell Sea origin. Wienders et al. (2000) used the 46.04 σ_4 isoline as the upper limit of WSDW in the SAO. Using the OMP results we can establish a third criterion: waters with a contribution higher than 50% of $WSDW_{-0.3}$ can be considered as part of the WSDW realm. Remember that the $WSDW_{-0.3}$ characteristics are not those in the Weddell Sea but the WSDW characteristics when it enters the SAO. In this study, this criterion can only be applied to line A17 line, as the $WSDW_{-0.3}$ along the A14 line was always lower than 45%.

Fig. 12a shows the vertical distribution of the TDD, 50% $WSDW_{-0.3}$, 46.04 σ_4 and 46.06 σ_4 isolines along line A17. South of 42°S the mean depth difference between the 50% $WSDW_{-0.3}$ and the 46.04 σ_4 was about 700 dbar, this difference was higher north of 10°S. In the Vema Channel (34°S) the three isolines practically overlapped. South of this channel the main contributor to the 50% $WSDW_{-0.3}$ isoline was CDW with values around 40%, while north of this latitude $NADW_2$ was the major contributor (Fig. 12b).

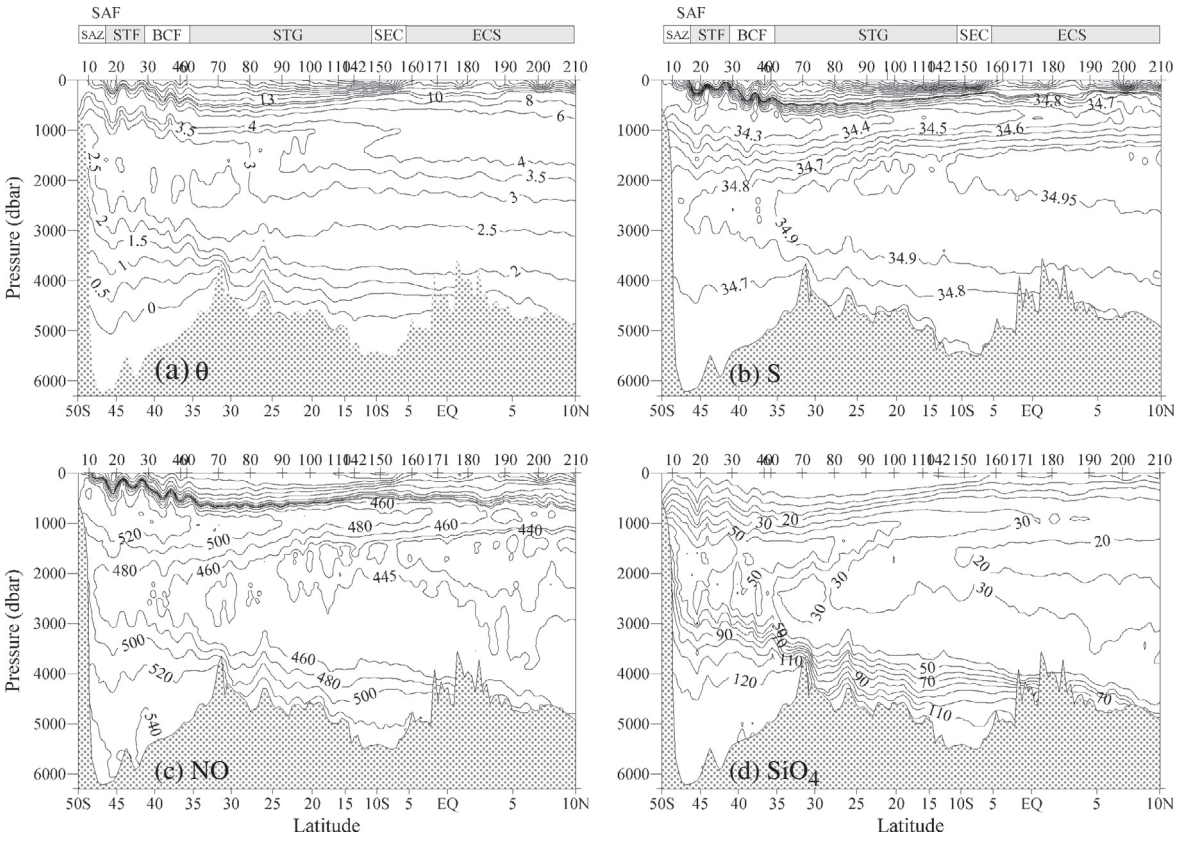

Fig. B2. Full-depth distributions of (a) potential temperature (θ, °C), (b) salinity (S, psu), (c) NO (μmol kg^{-1}) and (d) silicate (SiO4, μmol kg^{-1}) along WOCE line A17. SAF, Subantarctic Front or Malvinas Front in this case; SAZ, Subantarctic Zone; BCF, Brazil Current Front; STF, Subtropical Front; SEC, Subequatorial Current; ECS, Equatorial Current System.

The meridional evolution of σ_4 along the 50% $WSDW_{-0.3}$ isoline (Fig. 12c) shows an increase from 45.96 in the southern end to 45.99 in the northern end of line A17. The end member $WSDW_{-0.3}$ had a σ_4 density of 46.09, $NADW_2$ 45.88 and $CDW_{1.6}$ 45.81. Consequently, the northwards increase in density was due to the higher $NADW_2$ contribution towards the north. This density increase northwards evidences the existence of diapycnal mixing.

Finally, if we follow the $WSDW_{-0.3}$ contribution along the 46.04 σ_4 isoline (Fig. 12c) it is clear that the percentage was always higher than 50%: between 75% and 80% south of the Vema Channel and around 75% northwards. So, the 46.04 σ_4 isoline should not be used to define the WSDW realm but it would be preferably to use the 50% $WSDW_{-0.3}$ contribution.

5. Summary and conclusions

The present work is the first of two manuscripts with the general aim of studying the mineralization of biogenic materials within the realm of the variety of water masses that form, circulate and mix in the SAO. Here, an OMP analysis has been presented and assessed to solve the complex mixing of water masses in this basin using two densely-sampled lines in the western and eastern SAO, WOCE lines A17 and A14, respectively. This OMP analysis resolves weighted and dimensionless equations for the conservative parameters potential temperature, salinity, NO and silicate by means of NNLS. The amount of SWT (13) makes the system ill-posed if we are to use just the four equations plus mass conservation. Given the knowledge about water mass formation, circulation and mixing in the SAO we proposed several mixing figures to constrain the OMP. The sensitivity of this constrained OMP to several sources of error such as the variability in the SWT characteristics, the measured variables, the weighting factors and the R_N ratio was carefully assessed by means of perturbation tests. Taking into account that changing the weights has a minimum impact on the reliability and robustness of the OMP analysis and the resulting SWT distributions, and that SWT and data should be altered 4-fold relative to their typical uncertainty to detect changes in the OMP best solution, varying the R_N would be the only factor of uncertainty. However, even for the R_N perturbation tests, the mean absolute differences for any SWT were less than 5%.

The proposed constrained OMP analysis is robust and stable, being a relatively simple, interpretable and integrative tool to define the realms and cores-of-flow of the water masses of the SAO, going beyond the classical approach of following physical and/or chemical extremes or isopycnals. On the western and eastern SAO, Central Waters are modelled using four different SWT. Their meridional distribution is determined by the upper layer circulation (fronts, wind regimes and currents) in the SAO. Special complexity was found in the eastern SAO: EQ_{13} was the dominant Central Water mass in the ECS until 500 dbars, north of 5°S; while south of the SEC, the upper 200 dbars were occupied by SMW_{27} until the 28°S front separating subtropical from subequatorial waters; southwards, SACW-T_{18} and $STMW_{18}$ mixed in the upper 200 dbars, below EQ_{13}.

The main Intermediate Water mass in the SAO is AAIW. Its salinity minimum was detected all along both WOCE lines, but the oxygen maximum gradually vanished between 24°S and 14°S in line A17 and between 20°S and 25°S in line A14. The OMP helps to define the AAIW realm: contributions higher than 50% of AAIW

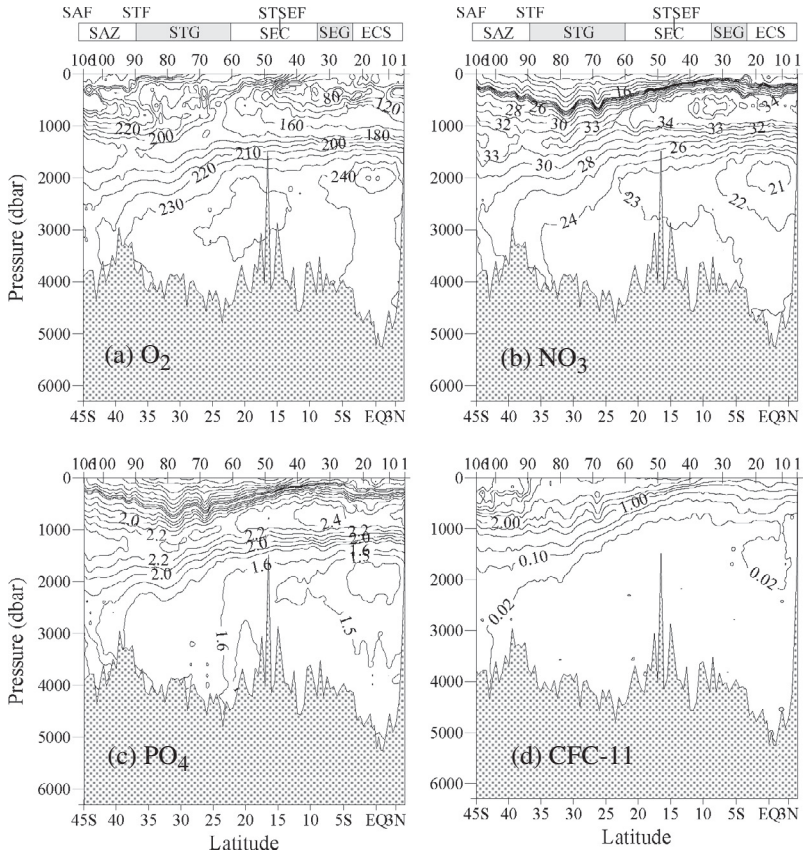

Fig. B3. Full-depth distributions of (a) dissolved oxygen (O2, μmol kg^{-1}), (b) nitrate (NO3, μmol kg^{-1}), (c) phosphate (PO4, μmol kg^{-1}) and (d) CFC-11 (pmol kg^{-1}) along WOCE line A14. SAF, Subantarctic Front; SAZ, Subantarctic Zone; STF, Subtropical Front; STG, Subtropical Gyre; SEC, Subequatorial Current; STSEF, Subtropical–Subequatorial front; SEG, Subequatorial gyre; ECS, Equatorial Current System.

were found south of the Equator for both WOCE lines. The physical and chemical characteristics of the core-of-flow of AAIW changed according to its complex circulation within the SAO and biogeochemical processes along the path.

The OMP setting is able to reproduce the CDW split into its lower and upper components within the SAO due to the confluence with the southward flowing NADW at ~26°S along both WOCE lines. The controversy about the silicate maximum north of 26°S around 1000 dbars is resolved: north of this latitude the main contributor to the UCDW maximum is AAIW (in 40%–50%) and explains the silicate maximum, previously attributed to UCDW.

The three components of NADW detected in the SAO were modelled using two SWT: $NADW_{4.6}$ represented the Upper and Middle NADW and $NADW_2$ modelled the Lower NADW. The $NADW_{4.6}$ maximum located around 1500 dbar until 23°S where it deepened to 2400 dbar at 35°S on both WOCE lines. This deepening relates to the UCDW encounter deflecting $NADW_{4.6}$ eastwards. The $NADW_2$ maximum located around 4000 dbar until 30°S where it began to shoal reaching 2000 dbar at the southern end of line A17. This relates with the encounter with WSDW within the Argentine Basin. Within this basin, both NADW branches practically converged and their chemical extremes were not longer distinguished. $NADW_2$ crossed to the eastern SAO through the Romanche and Chain Fracture Zones, so within the eastern SAO it occupied less volume.

The Two Degree Discontinuity (TDD) separating Deep Waters with a northern influence from Antarctic Deep Waters can be considered as the upper limit of AABW. The meridional evolution of the SWT fractions along the TDD revealed that $WSDW_{-0.3}$ and $NADW_{4.6}$ both in the east and west lines contribute less than 5% and 10%, respectively. In the western SAO the main contributor south of the Vema Channel (35°S) was CDW and north of it, it was $NADW_2$. In the eastern SAO, the main contributor south of the Walvis Ridge (39°S) was CDW and $NADW_2$ northwards. As previously noted, this constrained OMP is a powerful tool to define water mass realms. We propose the 50% $WSDW_{-0.3}$ (defined at the entry of the SAO) isoline as the upper limit of WSDW instead of any isopycnal (46.04 or 46.06 σ_4), where the $WSDW_{-0.3}$ fraction is around 75%.

Acknowledgements

The authors wish to thank the captain and the crew of R/V Maurice Ewing and R/V L'Atalante for their help during the cruise. We are very grateful to C.G. Castro and M.J. Pazó for their participation in nutrient measurements. Financial support from this work came from the Spanish CICYT contracts ANT93-1156-E and ANT94-1168-E and, and from the IFREMER contract No. 94 1430 087. X.A.A.S. and M.A. were supported by the Spanish Ministry of Science and Innovation (MALASPINA expedition, grant number CSD2008-00077). M.A. was funded by the grant ORCASEX (RYC-2006-001836), program *Ramón y Cajal* from the Spanish Ministry of Science and Technology.

Appendix A. Additional information about sensitivity/perturbation tests

See Figs. A1–A8.

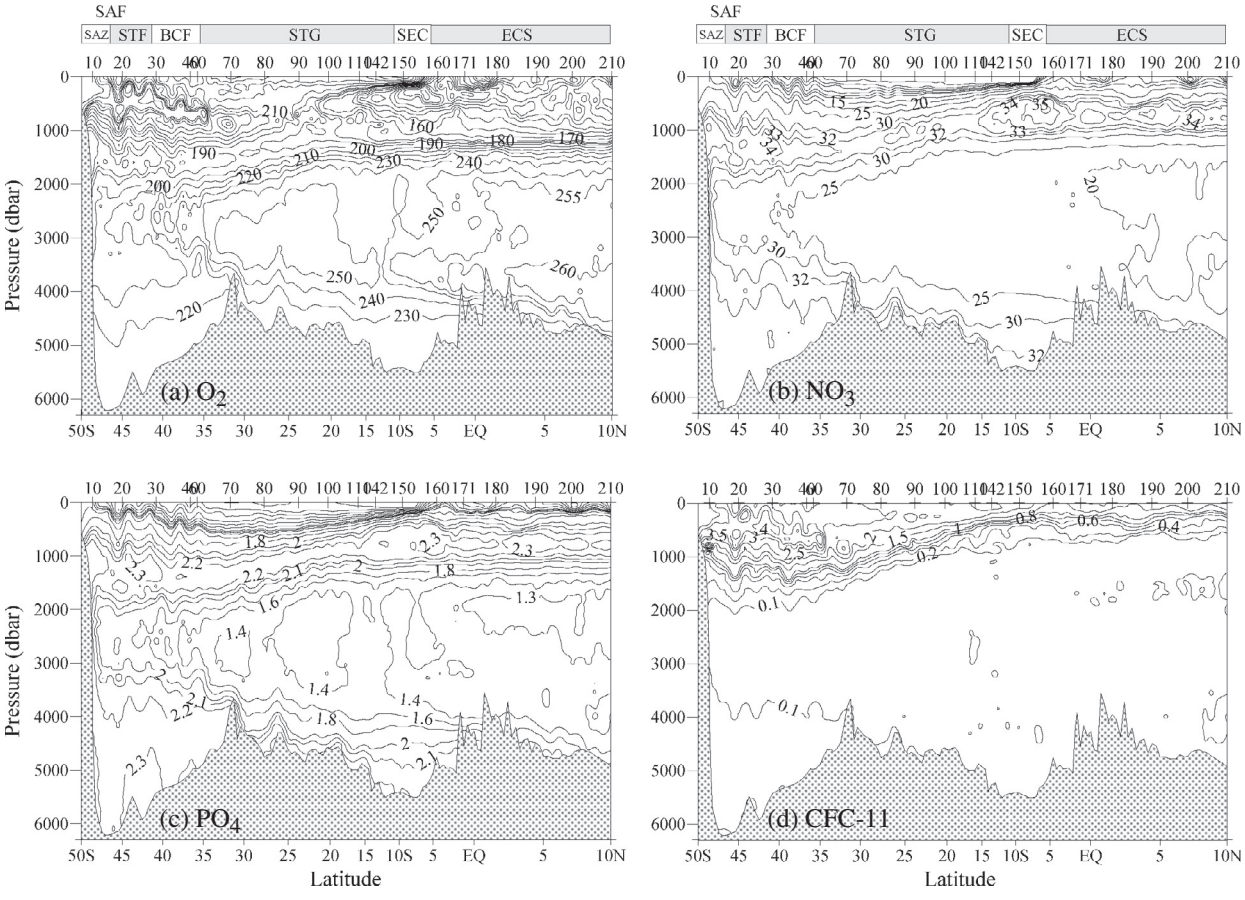

Fig. B4. Full-depth distributions of (a) dissolved oxygen (O2, μmol kg^{-1}), (b) nitrate (NO3, μmol kg^{-1}), (c) phosphate (PO4, μmol kg^{-1}) and (d) CFC-11 (pmol kg^{-1}) along WOCE line A17. SAF, Subantarctic Front or Malvinas Front in this case; SAZ, Subantarctic Zone; BCF, Brazil Current Front; STF, Subtropical Front; SEC, Subequatorial Current; ECS, Equatorial Current System.

Appendix B. Vertical distributions of physical and chemical variables along WOCE lines A14 and A17

See Figs. B1–B4.

References

Anderson, L.A., 1995. On the hydrogen and oxygen content of marine phytoplankton. Deep-Sea Research Part I 42, 1675–1680.

Anderson, L.A., Sarmiento, J.L., 1994. Redfield ratios of remineralization determined by nutrient data analysis. Global Biogeochemical Cycles 8, 65–80.

Andrié, C., Ternon, J.-F., Messias, M.-J., Mémery, L., Bourlès, B., 1998. Chlorofluoromethanes distributions in the deep equatorial Atlantic during January–March 1993. Deep-Sea Research Part I 45, 903–930.

Aoki, S., Hariyama, M., Mitsudera, H., Sasaki, H., Sasai, Y., 2007. Formation regions of Subantarctic Mode Water detected by OFES and Argo profiling floats. Geophysical Research Letters 34, L10606930. http://dx.doi.org/10.1029/2007GL029828.

Arhan, M., Mercier, H., Bourlès, B., Gouriou, Y., 1998. Hydrographic sections across the Atlantic at 7°30′N and 4°30′S. Deep-Sea Research Part I 45, 829–872.

Arhan, M., Heywood, K.J., King, B.A., 1999. The deep waters from the Southern Ocean at the entry of the Argentine Basin. Deep-Sea Research Part II 46, 475–499.

Arhan, M., Naveira Garabato, A.C., Heywood, K.J., Stevens, D.P., 2002. The Antarctic circumpolar current between the Falkland Islands and South Georgia. Journal of Physical Oceanography 32, 1914–1931.

Brea, S., Álvarez-Salgado, X.A., Álvarez, M., Pérez, F.F., Mémery, L., Mercier, H., Messias, M.J., 2004. Nutrient mineralization rates and ratios in the eastern South Atlantic. Journal of Geophysical Research 109, C05030. http://dx.doi.org/10.1029/2003JC002051.

Broecker, W.S., 1974. 'NO' a conservative water-mass tracer. Earth and Planetary Science Letters 23, 100–107.

Broecker, W.S., Takahashi, T., Li, Y.-H., 1976. Hydrography of the central Atlantic I. The two-degree discontinuity. Deep-Sea Research 23, 1083–1104.

Broecker, W.S., Takahashi, T., Takahashi, T., 1985. Sources and flow patterns of deep-ocean waters as deduced from potential temperature, salinity and initial phosphate concentration. Journal of Geophysical Research 90, 6925–6939.

Castro, C.G., Pérez, F.F., Holley, S.E., Rios, A.F., 1998. Chemical characterization and modelling of water masses in the Northeast Atlantic. Progress in Oceanography 41, 249–279.

Coles, V.J., McCartney, M.S., Olson, D.B., Smethie, W.M., 1996. Changes in Antarctic Bottom Water properties in the western South Atlantic in the late 1980s. Journal of Geophysical Research 101, 8957–8970.

Connary, S.D., Ewing, M., 1974. Penetration of Antarctic bottom water from the Cape Basin into the Angola Basin. Journal of Geophysical Research 79, 463–469.

de Brauwere, A., Jacquet, S.H.M., De Ridder, F., Dehairs, F., Pintelon, R., Schoukens, J., Baeyens W., 2007. Water mass distributions in the Southern Ocean derived from a parametric analysis of mixing water masses. Journal of Geophysical Research 112, C02021. http://dx.doi.org/10.1029/2006JC003742.

Durrieu De Madron, X., Weatherly, G., 1994. Circulation, transport and bottom boundary layers of the deep currents in the Brazil Basin. Journal of Marine Research 52, 583–638.

Edmond, J.M., Jacobs, S.S., Gordon, A.L., Mantyla, A.W., Weiss, R.F., 1979. Water column anomalies in dissolved silica over opaline pelagic sediments and the origin of the deep silica maximum. Journal of Geophysical Research 84, 7809–7826.

Ferron, B., Mercier, H., Speer, K.G., Gargett, A., Polzin, K., 1998. Mixing in the Romanche fracture zone. Journal of Physical Oceanography 28, 1929–1945.

Fraga, F., Ríos, A.F., Pérez, F.F., Figueiras, F.G., 1998. Theoretical limits of oxygencarbon and oxygennitrogen ratios during photosynthesis and the mineralization of the organic matter in the sea. Scientia Marina 62, 161–168.

Friedrichs, M.A.M., McCartney, M.S., Hall, M.M., 1994. Hemispheric asymmetry of deep water transport modes in the western Atlantic. Journal of Geophysical Research 99, 25165–25179.

Georgi, D.T., 1981. On the relationships between the large-scale property variations and fine structures of the Antarctic Circumpolar Current. Journal of Geophysical Research 86, 6556–6566.

Gordon, A.L., 1981. South Atlantic thermocline ventilation. Deep-Sea Research Part A 28, 1239–1264.

Gordon, A.L., Bosley, K.T., 1991. Cyclonic gyre in the tropical south Atlantic. Deep-Sea Research Part A 38 (Suppl.), S323–S343.

Gouretski, V.V., Jancke, K., 2001. Systematic errors as the cause for an apparent deep water property variability global analysis of the WOCE and historical hydrographic data. Progress in Oceanography 48, 337–402.

Groupe CITHER-2, 1995. Recueil de données, Campagne CITHER 2, N/O Maurice Ewing (4 janvier-21 mars 1994), vol. 2, CTD-O2, Rapport Interne LPO 95-04, Laboratoire de Physique des Océans/IFREMER, Centre de Brest, Plouzané, France, 520 pp.

Groupe CITHER-2, 1996a. Recueil de données, Campagne CITHER 2, N/O Maurice Ewing (4 janvier-21 mars 1994), vol. 1, Mesures "en route", paramètres météorologiques, bathymétrie et courantométrie Doppler, Rapport Interne LPO 96-01, Laboratoire de Physique des Océans/IFREMER, Centre de Brest, Plouzané, France, 180 pp.

Groupe CITHER-2, 1996b. Recueil de données, Campagne CITHER 2, N/O Maurice Ewing (4 janvier-21 mars 1994), vol. 3, Traceurs géochimiques, Rapport Interne LPO 96-02, Laboratoire de Physique des Océans/IFREMER, Centre de Brest, Plouzané, France, 560 pp.

Groupe CITHER-3, 1996. Recueil de données, Campagne CITHER 3, N/O L'Atalante (11 janvier-2 avril 1995), vol. 2, CTD-O2, Rapport Interne LPO 96–05, Laboratoire de Physique des Océans/IFREMER, Centre de Brest, Plouzané, France, 532 pp.

Groupe CITHER-3, 1998. Recueil de données, Campagne CITHER 3, N/O L'Atalante (11 janvier-2 avril 1995), vol. 3, Traceurs Géochimiques, Rapport Interne LPO 98-03, Laboratoire de Physique des Océans/IFREMER, Centre de Brest, Plouzané, France, 586 pp.

Hanawa, K., Talley, L.D., 2001. Mode waters. In: Siedler, G., Church, J. (Eds.), Ocean Circulation and Climate. International Geophysics Series. Academic Press, pp. 373–386.

Henry-Edwards, A., Tomczak, M., 2006. Remote detection of water property changes from a time series of oceanographic data. Ocean Science 2, 11–18.

Hogg, N.G., Owens, W.B., 1999. Direct measurement of the deep circulation within the Brazil Basin. Deep-Sea Research Part II 46, 335–353.

Holfort, J., Siedler, G., 2001. The meridional oceanic transport of heat and nutrients in the South Atlantic. Journal of Physical Oceanography 31, 5–29.

Hoppema, M., Velo, A., van Heuven, S., Tanhua, T., Key, R.M., Lin, X., Bakker, D.C.E., Perez, F.F., Ríos, A.F., Lo Monaco, C., Sabine, C.L., Álvarez, M., Bellerby, R.G.J., 2009. Consistency of cruise data of the CARINA database in the Atlantic sector of the Southern Ocean. Earth System Science Data 1, 63–75.

Hupe, A., Karstensen, J., 2000. Redfield stoichiometry in Arabian Sea subsurface waters. Global Biogeochemical Cycles 14, 357–372.

Johnson, G.C., 2008. Quantifying Antarctic bottom water and North Atlantic deep water volumes. Journal of Geophysical Research 113, C05027. http://dx.doi.org/10.1029/2007JC004477.

Karstensen, J., Tomczak, M., 1998. Age determination of mixed water masses using CFC and oxygen data. Journal of Geophysical Research 103 (C9), 18599–18609.

Key, R.M., Kozyr, A., Sabine, C.L., Lee, K., Wanninkhof, R., Bullister, J., Feely, R.A., Millero, F., Mordy, C., Peng, T.-H., 2004. A global ocean carbon climatology Results from GLODAP. Global Biogeochemical Cycles 18, 4031.

Key, R.M., Tanhua, T., Olsen, A., Hoppema, M., Jutterström, S., Schirnick, C., van Heuven, S., Kozyr, A., Lin, X., Velo, A., Wallace, D.W.R., Mintrop, L., 2010. The CARINA data synthesis project introduction and overview. Earth System Science Data 2, 105–624.

Larqué, L., Maamaatuaiahutapu, K., Garçon, V., 1997. On the intermediate and deep water flows in the South Atlantic Ocean. Journal of Geophysical Research 102, 12425–12440.

Laws, E.A., 1991. Photosynthetic quotients, new production and net community production in the open ocean. Deep-Sea Research Part A 38, 143–167.

Lawson, C.L., Hanson, R.J., 1974. Solving Least Squares Problems. Prentice-Hall, Englewood Cliffs, NJ.

Marsh, R., Nurser, A.J.G., Megann, A.P., New, A.L., 2000. Water mass transformation in the Southern Ocean of a global isopycnal coordinate GCM. Journal of Physical Oceanography 30, 1013–1045.

McCartney, M.S., 1977. Subantarctic mode water. In: A Voyage of Discovery George Deacon 70th Anniversary Volume. Deep-Sea Research 24 (Suppl.), 103–119.

McCartney, M.S., 1982. The subtropical recirculation of mode waters. Journal of Marine Research 40, 427–464.

McCartney, M.S., 1993. Crossing of the equator by the deep western boundary current in the western Atlantic Ocean. Journal of Physical Oceanography 23, 1953–1974.

McCartney, M.S., Curry, R.A., 1993. Transequatorial flow of Antarctic Bottom Water in the western Atlantic Ocean: abyssal geostrophy at the equator. Journal of Physical Oceanography 23, 1264–1276.

Mémery, L., Arhan, M., Álvarez-Salgado, X.A., Messias, M.-J., Mercier, H., Castro, G.C., Ríos, A.F., 2000. The water masses along the western boundary of the South and Equatorial Atlantic. Progress in Oceanography 47, 69–98.

Mercier, H., Morin, P., 1997. Hydrography of the Romanche and Chain fracture zones. Journal of Geophysical Research 102, 10373–10389.

Mercier, H., Speer, K.G., 1998. Transport of bottom water in the Romanche Fracture Zone and the Chain Fracture Zone. Journal of Physical Oceanography 28, 779–790.

Montgomery, R.B., 1958. Water characteristics of Atlantic Ocean and World Ocean. Deep-Sea Research 5, 134–148.

Olson, D.B., Podestá, G.P., Evans, R.H., Brown, O.B., 1988. Temporal variations in the separation of Brazil and Malvinas Currents. Deep-Sea Research Part A 35, 1971–1990.

Onken, R., 1995. The spreading of lower circumpolar deep water into the Atlantic Ocean. Journal of Physical Oceanography 25, 3051–3063.

Orsi, A.H., Johnson, G.C., Bullister, J.L., 1999. Circulation, mixing, and production of Antarctic Bottom Water. Progress in Oceanography 43, 55–109. http://dx.doi.org/10.1016/S0079-6611(99)00004-X.

Oudot, C., Morin, P., Baurand, F., Wafer, M., Le Corre, P., 1998. Northern and southern water masses in the equatorial Atlantic distribution of nutrients on the WOCE A6 and A7 lines. Deep-Sea Research Part I 45, 873–902.

Pérez, F.F., Mintrop, L., Llinás, O., Glez-Davila, M., Castro, C.G., Álvarez, M., Koertzinger, A., Santana-Casiano, M., Ríos, A.F., 2001. Mixing analysis of nutrients, oxygen and inorganic carbon in the Canary Islands region. Journal of Marine Systems 28, 183–201.

Peterson, R.G., Stramma, L., 1991. Upper-level circulation in the South Atlantic Ocean. Progress in Oceanography 26, 1–73.

Peterson, R.G., Whitworth, T.I.I.I., 1989. The Subantarctic and Polar Fronts in relation to deep water masses through the southwestern Atlantic. Journal of Geophysical Research 94, 10817–10838.
Piola, A.R., Gordon, A.L., 1989. Intermediate waters in the southwest South Atlantic. Deep-Sea Research Part A 36, 1–16.
Poole, R., Tomczak, M., 1999. Optimum multiparameter analysis of the water mass structure in the Atlantic Ocean thermocline. Deep-Sea Research Part I 46, 1895–1921.
Provost, C., Escoffier, C., Maamaatuaiahutapu, K., Kartavtseff, A., Garçon, V., 1999. Subtropical mode waters in the South Atlantic Ocean. Journal of Geophysical Research 104, 21033–21049.
Reid, J.L., 1989. On the total geostrophic circulation of the South Atlantic Ocean flow patterns, tracers, and transports. Progress in Oceanography 23, 149–244.
Reid, J.L., 1996. On the circulation of the South Atlantic. In: Wefer, G., Berger, W.H., Siedler, G., Webb, D.J. (Eds.), The South Atlantic Present and Past Circulation. Springer-Verlag, NY, pp. 13–44.
Roden, G.I., 1986. Thermohaline fronts and baroclinic flow in the Argentine basin during the austral spring of 1984. Journal of Geophysical Research 91, 5075–5093.
Smythe-Wright, D., Boswell, S., 1998. Abyssal circulation in the Argentine Basin. Journal of Geophysical Research 103, 15845–15851.
Speer, K.G., McCartney, M.S., 1992. Bottom water circulation in the western North Atlantic. Journal of Physical Oceanography 22, 83–92.
Speich, S., Blanke, B., de Vries, P., Drijfhout, S., Döös, K., Ganachaud, A., Marsh, R., 2002. Tasman leakage: a new route in the global ocean conveyor belt. Geophysical Research Letters 29. http://dx.doi.org/10.1029/2001GL014586.
Stramma, L., England, M., 1999. On the water masses and mean circulation of the South Atlantic Ocean. Journal of Geophysical Research 104, 20863–20883.
Stramma, L., Schott, F., 1999. The mean flow field of the tropical Atlantic Ocean. Deep-Sea Research Part I 46, 279–303.
Suga, T., Talley, L.D., 1995. Antarctic Intermediate Water circulation in the tropical and subtropical South Atlantic. Journal of Geophysical Research 100, 13441–13453.
Talley, L.D., 1996. Antarctic intermediate water in the South Atlantic. In: Wefer, G. et al. (Eds.), The South Atlantic Present and Past Circulation. Springer Verlag, pp. 219–238.
Tanhua, T., van Heuven, S., Key, R.M., Velo, A., Olsen, A., Schirnick, C., 2010. Quality control procedures and methods of the CARINA database. Earth System Science Data 2, 35–40.
Thomas, H., Ittekkot, V., 2001. Determination of anthropogenic CO_2 in the North Atlantic ocean using water mass ages and CO_2 equilibrium chemistry. Journal of Marine Systems 27 (2001), 325–336.
Tomczak, M., 1981. A multi-parameter extension of temperature/salinity diagram techniques for the analysis of non-isopycnal mixing. Progress in Oceanography 10, 147–171.
Tomczak, M., 1999. Some historical, theoretical and applied aspects of quantitative water mass analysis. Journal of Marine Research 57, 275–303.
Tomczak, M., Godfrey, J.S., 2003. Regional Oceanography an Introduction. Pergamon Press, 422 pp.
Tomczak, M., Large, D.G.B., 1989. Optimum multiparameter analysis of mixing in the thermocline of the eastern Indian Ocean. Journal of Geophysical Research 94, 16141–16149.
Tsuchiya, M., 1986. Thermostads and circulation in the upper layer of the Atlantic Ocean. Progress in Oceanography 16 (4), 235–267.
Tsuchiya, M., Talley, L.D., McCartney, M.S., 1994. Water-mass distributions in the western South Atlantic a section from South Georgia Island (54°S) northward across the Equator. Journal of Marine Research 52, 55–81.
Vanicek, M., Siedler, G., 2002. Zonal fluxes in the deep water layers of the western South Atlantic Ocean. Journal of Physical Oceanography 32, 2205–2235.
Warner, J.M., Weiss, R.F., 1992. Chlorofluoromethanes in South Atlantic Antarctic intermediate water. Deep-Sea Research Part A 39, 2053–2075.
Weiss, R.F., Bullister, J.L., Gammon, R.H., Warner, M.J., 1985. Atmospheric chlorofluoromethanes in the deep equatorial Atlantic. Nature 314, 608–610.
Whitworth III, T., Nowlin Jr., W.D., 1987. Water masses and currents of the southern ocean at the Greenwich Meridian. Journal of Geophysical Research 92, 6462–6476.
Wienders, N., Arhan, M., Mercier, H., 2000. Circulation at the western boundary of the South and Equatorial Atlantic. Exchanges with the ocean interior. Journal of Marine Research 58, 1007–1039.
Worthington, L.V., 1976. On the North Atlantic circulation, Johns Hopkins Oceanographic Studies, vol. 6. John Hopkins University Press, Baltimore, MD, 110 pp.
Worthington, L.V., Metcalf, W.G., 1961. The relationship between potential temperature and salinity in the deep Atlantic Water, Conseil International pour l'Exploration de la Mer (CIEM). Rapports et Procès-Verbaux des Réunions 149, 122–128.
Wüst, G., 1935. Schichtung und Zirkulation des Atlantischen Ozeans, Die Stratosphäre. Wissenschaftliche Ergebnisse der Deutschen Atlantischen Expedition auf dem Forschungsund Vermessungsschiff "Meteor" 1925–1927. 6, 180 pp. (English translation edited by W.J. Emery, The stratosphere of the Atlantic Ocean. Scientific Results of the German Atlantic Expedition of the Research Vessel 'Meteor' 1925–27. Amerind Publishing Co., 1978).
You, Y., 1997. Seasonal variations of thermocline circulation and ventilation in the Indian Ocean. Journal of Geophysical Research 102 (C5), 10391–10422.